

# The Turbulent Destruction of Clouds - II. Mach Number Dependence, Mass-loss Rates, and Tail Formation

J. M. Pittard<sup>1\*</sup>, T. W. Hartquist<sup>1</sup>, and S. A. E. G. Falle<sup>2</sup>

<sup>1</sup>*School of Physics and Astronomy, The University of Leeds, Leeds LS2 9JT, UK*

<sup>2</sup>*Department of Applied Mathematics, The University of Leeds, Leeds LS2 9JT, UK*

Accepted 2010 February 10. Received 2010 February 10; in original form 2009 September 22

## ABSTRACT

The turbulent destruction of a cloud subject to the passage of an adiabatic shock is studied. We find large discrepancies between the lifetime of the cloud and the analytical result of Hartquist et al. (1986). These differences appear to be due to the assumption in Hartquist et al. (1986) that mass-loss occurs largely as a result of lower pressure regions on the surface of the cloud away from the stagnation point, whereas in reality Kelvin-Helmholtz (KH) instabilities play a dominant role in the cloud destruction. We find that the true lifetime of the cloud (defined as when all of the material from the core of the cloud is well mixed with the intercloud material in the hydrodynamic cells) is about  $6 \times t_{\text{KHD}}$ , where  $t_{\text{KHD}}$  is the growth timescale for the most disruptive, long-wavelength, KH instabilities. These findings have wide implications for diffuse sources where there is transfer of material between hot and cool phases.

The properties of the interaction as a function of Mach number and cloud density contrast are also studied. The interaction is milder at lower Mach numbers with the most marked differences occurring at low shock Mach numbers when the postshock gas is subsonic with respect to the cloud (i.e.  $M < 2.76$ ). Material stripped off the cloud only forms a long “tail-like” feature if  $\chi \gtrsim 10^3$ .

**Key words:** hydrodynamics – ISM: clouds – ISM: kinematics and dynamics – shock waves – supernova remnants – turbulence

## 1 INTRODUCTION

The interchange of material between dense cool phases and a hotter, more tenuous, external medium is a key phenomenon in astrophysics which influences the morphology and evolution of diffuse sources over a wide range of spatial and energy scales. Clouds (also referred to as clumps, globules, and knots) may either accumulate material from, or lose material to, the surrounding medium. In the latter case, mass-loss can occur through hydrodynamic ablation, or thermal or photoionized evaporation (see, e.g., Pittard 2007, and references therein). The response of such multi-phase environments to the impact of winds and shocks is central to the investigation of feedback in star and galaxy formation, and encompasses objects such as tails behind mass-losing stars (e.g. Martin et al. 2007), planetary nebulae (e.g. Matsuura et al. 2009), supernova remnants (e.g. Danforth, Blair & Raymond 2001; Levenson, Graham & Walters 2002), starburst regions (e.g. Westmoquette et al. 2007, 2009), starburst superwinds (e.g.

Strickland et al. 2000; Cecil, Bland-Hawthorn & Veilleux 2002; Veilleux, Cecil & Bland-Hawthorn 2005), and the intracluster medium (e.g. Conselice, Gallagher & Wyse 2001).

Such interactions have been extensively investigated using numerical hydrodynamics over the last two decades. A large literature of shock-cloud, wind-cloud, and jet-cloud interactions now exists. In it, the effects of radiative cooling, thermal conduction, and ordered magnetic fields have all been considered. These studies have provided great insight into the behaviour and evolution of clouds subject to a variety of internal and external conditions. However, all suffer from a common and fundamental problem. In most astrophysical environments the interaction of shocks, winds, and jets with clouds takes place at high Reynolds numbers and is turbulent (see Pittard et al. 2009, for a review of the key physics). Unfortunately, the formation of fully developed turbulence is prevented by the artificial viscosity inherent in the hydrodynamical simulations. The turbulent mixing of cloud material into the surrounding medium is therefore limited, and the destruction of the cloud is hindered.

The only tractable solution to this problem is to use a statistical approach to describe the turbulent flow. One pos-

\* E-mail: jmp@ast.leeds.ac.uk

sible method involves the use of a subgrid turbulent viscosity model, designed to calculate the properties of the turbulence and the resulting increase in the transport coefficients that the turbulence brings. In this way, the subgrid turbulence model emulates a high Reynolds number flow. An initial investigation by Pittard et al. (2009) of an adiabatic, Mach 10, shock-cloud interaction found increasing and significant differences between the results from a  $k$ - $\epsilon$  turbulence model and an inviscid model as the density contrast between the cloud and inter-cloud medium,  $\chi$ , increased past  $10^2$ . In addition, the  $k$ - $\epsilon$  turbulence model demonstrated better convergence in resolution tests, a feature which is particularly useful for simulations involving multiple clouds. The effect of a turbulent, as opposed to a laminar, post-shock medium sweeping over the cloud was also investigated. The strong “buffeting” that the cloud receives in this case results in its significantly quicker destruction.

It is also surprising that previous shock-cloud studies have focussed almost exclusively on high Mach number interactions (see Table 1). Where lower Mach numbers have been considered (e.g., Fragile et al. 2004; Nakamura et al. 2006), a detailed comparison to higher Mach number interactions is lacking. In this work we extend the shock-cloud investigation of Pittard et al. (2009) by examining the Mach number dependence of the interaction. We compare our numerical results against the analytical mass-loss rate formula of Hartquist et al. (1986), and for the first time investigate in detail how well it describes the rate of destruction of the cloud. We also determine the conditions which are required for a long identifiable tail to be created behind the cloud.

The structure of this paper is as follows. In Section 2 the numerical method and analysis are introduced. Section 3 notes the main stages in the destruction of a cloud by a high Mach number shock, and the Mach-scaling of the interaction is discussed. Our results are presented in Section 4, where a variety of simulations for strong and weak shocks are presented and compared. Section 5 summarizes and concludes this work.

## 2 THE NUMERICAL SETUP

The calculations were performed in 2D axisymmetry using an Eulerian adaptive mesh refinement (AMR) hydrodynamic code, with a linear Godunov solver and piece-wise linear cell interpolation (see Falle 1991). The entire computational domain is covered by the two coarsest grids,  $G^0$  and  $G^1$ . The solution at each position is calculated on all grids that exist there, and the difference between these solutions is used to control refinement. 8 grid levels were used in total, with a factor of 2 refinement between each. In all simulations the coarse-grid resolution is equal to the radius of the cloud, with 128 cells per cloud radius on the finest grid. An advected scalar is used to distinguish between cloud and ambient material.

The interaction is simplified by adopting a number of assumptions. The magnetic field is assumed to be too weak to be dynamically important. We also assume that radiative cooling can be ignored. This is valid if the cloud is small enough, and preserves the scale-free nature of the simulations. The efficiency of thermal conduction in magnetized turbulent plasmas remains highly uncertain (see

Pittard et al. 2009, and references therein), and for simplicity its effects are also ignored here. Finally, we also ignore self-gravity. It is unimportant in a cloud struck by a strong adiabatic shock (Klein et al. 1994), but should be included in future work on mildly supersonic shock cloud interactions.

The turbulence in the sub-grid  $k$ - $\epsilon$  model is assumed to be fully developed, and has been calibrated by comparing the computed growth of shear layers with experiments (Dash & Wolf 1983). Turbulent energy ( $k$ , per unit mass) is generated by the action of the turbulent viscosity on the mean flow and is converted to heat at the dissipation rate per unit mass,  $\epsilon$ . Since the turbulent energy resides mainly in large eddies, while the dissipation occurs in the small ones, one can think of  $k$  and  $\epsilon$  as describing the large-scale and small-scale turbulence respectively. Further details of the model implementation including the full set of equations that are solved can be found in Pittard et al. (2009).

The ratio of the turbulent and thermal energy densities,  $e_{tb}/e_{th}$ , is  $\sim 10^{-6}$  in the initial post-shock flow. Within the pre-shock medium (including the cloud), we set  $e_{tb}/e_{th} = 0.04$ . These values are low enough to not affect the initial dynamics of the interaction, and are identical to those used by Pittard et al. (2009) in their investigation of a Mach 10 shock-cloud interaction (where much higher levels of post-shock turbulence were also investigated).

The numerical domain is set large enough so that the cloud is well dispersed and mixed into the post-shock flow before the shock reaches its edge. In this way various global quantities detailed below can be accurately computed. The shock propagates parallel to the axis of symmetry, which is the  $z$ -axis. For clouds with a density contrast  $\chi = 10^3$  with respect to the ambient medium, the grid had an extent of  $0 \leq r \leq 24$ , with  $-910 \leq z \leq 290$  when  $M = 1.5$ ,  $-510 \leq z \leq 20$  when  $M = 3$ , and  $-510 \leq z \leq 6$  when  $M = 10$ , where the unit of length corresponds to a cloud radius,  $r_c$ . Smaller grids were used when  $\chi$  was lower. All calculations were performed for an ideal gas with  $\gamma = 5/3$ , and were scaled so that the fluid variables have values reasonably close to unity.

Clouds in the ISM do not have infinitely sharp edges, so we adopt the density profile specified in Pittard et al. (2009):

$$\rho(r) = \rho_{amb}[\psi + (1 - \psi)\eta], \quad (1)$$

where

$$\eta = \frac{1}{2} \left( 1 + \frac{\alpha - 1}{\alpha + 1} \right), \quad (2)$$

$\alpha = \exp \{ \min[20.0, p_1((r/r_c)^2 - 1)] \}$ , and  $r$  is the distance from the centre of the cloud.  $\psi$  is adjusted to obtain a specific density contrast for the centre of the cloud with respect to the ambient medium ( $\chi = \rho_{max}/\rho_{amb}$ ). The parameter  $p_1$  controls the steepness of the profile at the edge of the cloud. We set  $p_1 = 10$  (i.e. a sharp-edged cloud), and place the cloud in pressure equilibrium with its surroundings.

The evolution of the interaction is studied through various integrated quantities (see Klein et al. 1994; Nakamura et al. 2006; Pittard et al. 2009). These include the effective radii of the cloud normal to and along the axis of symmetry ( $a$  and  $c$ , respectively), its mass ( $m$ ), its mean velocity ( $\langle v_x \rangle$ , measured in the frame of the unshocked cloud), the velocity dispersions in the radial and axial

**Table 1.** A representative (but incomplete) summary of previous numerical investigations of shock-cloud and wind-cloud interactions.  $\chi$  is the density contrast of the cloud with respect to the ambient medium and  $M$  is the shock Mach number. The interaction types are: SCS = shock-cloud (single); SCM = shock-cloud (multiple); WCS = wind-cloud (single). The references are as follows: <sup>a</sup>Stone & Norman (1992); <sup>b</sup>Klein et al. (1994); <sup>c</sup>Mac Low et al. (1994); <sup>d</sup>Mellema, Kurk & Röttgering (2002); <sup>e</sup>Fragile et al. (2004); <sup>f</sup>Orlando et al. (2005); <sup>g</sup>Nakamura et al. (2006); <sup>h</sup>van Loo et al. (2007); <sup>i</sup>Orlando et al. (2008); <sup>j</sup>Shin et al. (2008); <sup>k</sup>Poludnenko et al. (2002); <sup>l</sup>Gregori et al. (2000); <sup>m</sup>Poludnenko et al. (2004); <sup>n</sup>Marcolini et al. (2005); <sup>o</sup>Raga et al. (2007); <sup>p</sup>Vieser & Hensler (2007).

Authors	Interaction type	Geometry	Typical (max) resolution	$\chi$	$M$	Cooling?	Conduction?	Magnetic fields?
SN92 <sup>a</sup>	SCS	3D XYZ	60 (60)	10	10			
KMC94 <sup>b</sup>	SCS	2D RZ	120 (240)	3,10,30,100,400	10,100,1000			
MC94 <sup>c</sup>	SCS	2D RZ,XY	50 (240)	10	10,100			✓
MKR02 <sup>d</sup>	SCS	2D RZ,XY	200 (200)	1000	10	✓		
F04 <sup>e</sup>	SCS	2D XY	200 (200)	1000	5,10,20,40	✓		
O05 <sup>f</sup>	SCS	2D RZ, 3D XYZ	132 (132)	10	30,50	✓	✓	
N06 <sup>g</sup>	SCS	2D RZ, 3D XYZ	120 (960)	10,100	1.5,10,100,1000			
V07 <sup>h</sup>	SCS	2D RZ	640 (640)	45	1.5,2.5,5	✓		✓
O08 <sup>i</sup>	SCS	2.5D XYZ	132 (528)	10	50	✓	✓	✓
SSS08 <sup>j</sup>	SCS	3D XYZ	68 (68)	10	10			✓
PFB02 <sup>k</sup>	SCM	2D XY	32 (32)	500	10			
G00 <sup>l</sup>	WCS	3D XYZ	16 (26)	10,30,100	1.5,3			✓
PFM04 <sup>m</sup>	WCS	2D RZ	128 (128)	100	10-200	✓		
M05 <sup>n</sup>	WCS	2D RZ	150 (150)	100,500	3,6,67	✓	✓	
R07 <sup>o</sup>	WCS	3D XYZ	77 (77)	10	242	✓		
VH07 <sup>p</sup>	WCS	2D RZ	33 (51)	0.6,1.2, $6.1 \times 10^4$	0.3	✓	✓	

Notes: Patnaude & Fesen (2005) and Cooper et al. (2009) consider a cloud with substructure. Multiple-cloud interactions were also considered by Fragile et al. (2004) and Melioli et al. (2005), though this was not the main focus of their work. Simulations with continuous mass-injection (to mimic the destruction of very long lived clouds) have been presented by Falle et al. (2002), Pittard et al. (2005), Dyson et al. (2006), and Pope et al. (2008). Pittard et al. (2005) investigated the interaction of a wind with multiple mass-injection sources.

**Table 2.** The dependences of the global cloud and core properties on the shock Mach number in subgrid turbulence calculations with cloud density contrasts of  $\chi = 10$  (models “c1”),  $\chi = 10^2$  (models “c2”), and  $\chi = 10^3$  (models “c3”). The Mach number for each model is given by the number following the initial “m” in the model name - calculations with Mach numbers of 1.5, 2, 3, 4, 6, 10, and 40 were made. The time-dependent quantities are evaluated at  $t = t_{\text{mix}}$  (cf. Pittard et al. 2009). Values in parentheses are obtained from integrations over the “core” mass rather than the “cloud” mass.

Model	$t_{\text{drag}}/t_{\text{cc}}$	$t_{\text{mix}}/t_{\text{cc}}$	$a/r_{\text{c}}$	$c/r_{\text{c}}$	$c/a$	$\langle \rho \rangle / \rho_{\text{max}}$	$\langle v_z \rangle / v_{\text{b}}$
m1.5c1	2.97 (3.04)	(10.3)	1.90 (1.97)	2.76 (2.74)	1.45 (1.39)	0.364 (0.543)	0.292 (0.305)
m2c1	1.94 (1.98)	(7.95)	1.71 (1.78)	2.68 (2.79)	1.57 (1.57)	0.452 (0.655)	0.404 (0.432)
m3c1	1.40 (1.47)	(6.54)	1.52 (1.35)	2.55 (2.75)	1.68 (2.03)	0.580 (0.909)	0.471 (0.472)
m4c1	1.18 (1.25)	(6.11)	1.67 (1.58)	2.46 (2.37)	1.47 (1.50)	0.649 (1.008)	0.541 (0.537)
m6c1	1.04 (1.13)	(6.10)	1.77 (1.78)	2.54 (2.70)	1.44 (1.51)	0.641 (0.883)	0.604 (0.629)
m10c1	1.04 (1.11)	(5.96)	1.66 (1.74)	2.20 (2.40)	1.33 (1.38)	0.680 (1.030)	0.579 (0.629)
m40c1	0.91 (1.01)	(6.20)	1.78 (1.89)	2.26 (2.42)	1.27 (1.28)	0.692 (1.044)	0.599 (0.657)
m1.5c2	6.04 (14.0)	(8.41)	2.68 (1.46)	9.63 (1.57)	3.59 (1.07)	0.046 (0.197)	0.195 (0.111)
m2c2	4.43 (4.70)	(6.70)	3.11 (2.96)	8.75 (3.35)	2.81 (1.13)	0.051 (0.109)	0.354 (0.307)
m3c2	3.61 (3.78)	(6.04)	4.32 (4.64)	6.90 (1.79)	1.60 (0.38)	0.056 (0.129)	0.511 (0.490)
m4c2	3.44 (3.49)	(5.55)	4.09 (4.40)	5.29 (2.20)	1.29 (0.50)	0.063 (0.121)	0.536 (0.535)
m6c2	3.27 (3.32)	(4.98)	3.95 (3.28)	4.62 (1.98)	1.17 (0.60)	0.073 (0.181)	0.591 (0.517)
m10c2	3.08 (3.09)	(4.86)	3.92 (3.35)	4.12 (3.05)	1.05 (0.91)	0.075 (0.142)	0.593 (0.554)
m40c2	2.96 (3.01)	(4.63)	3.88 (3.64)	4.04 (2.29)	1.04 (0.63)	0.077 (0.163)	0.586 (0.542)
m1.5c3	9.19 (29.7)	(13.3)	5.20 (1.66)	65.5 (4.20)	12.6 (2.53)	0.0038 (0.029)	0.199 (0.073)
m2c3	8.66 (13.1)	(10.5)	3.42 (2.55)	57.4 (5.86)	16.8 (2.29)	0.0051 (0.019)	0.263 (0.142)
m3c3	7.92 (9.73)	(10.3)	4.31 (4.52)	67.5 (9.96)	15.7 (2.21)	0.0054 (0.012)	0.430 (0.360)
m4c3	6.98 (10.2)	(8.34)	3.40 (2.30)	61.2 (6.07)	18.0 (2.64)	0.0069 (0.027)	0.394 (0.213)
m6c3	6.07 (6.72)	(6.95)	4.19 (3.78)	42.1 (5.02)	10.1 (1.33)	0.0073 (0.019)	0.449 (0.333)
m10c3	6.84 (7.15)	(7.83)	4.01 (2.82)	49.1 (6.88)	12.2 (2.44)	0.0078 (0.025)	0.430 (0.271)
m40c3	5.29 (5.63)	(6.10)	4.47 (4.29)	31.1 (5.52)	6.95 (1.29)	0.0078 (0.018)	0.467 (0.366)

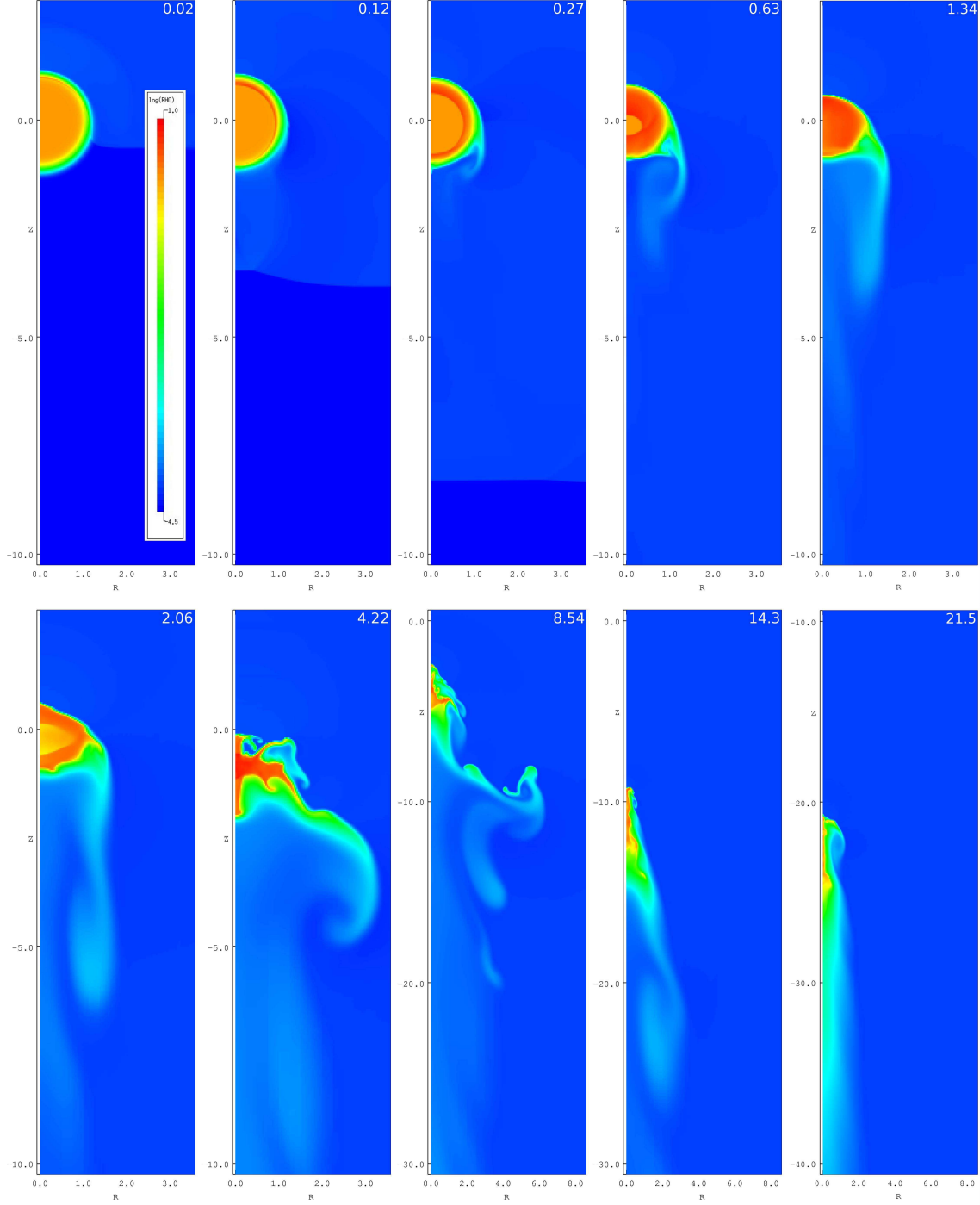


**Figure 1.** Snapshots of the density distribution from a  $k$ - $\epsilon$  calculation of a Mach 1.5 adiabatic shock hitting a cloud with a density contrast of  $10^3$  with respect to the ambient medium (model m1.5c3). The evolution proceeds left to right and top to bottom with  $t = 0.02, 0.12, 0.27, 0.63, 1.34, 2.06, 4.22, 8.54, 14.3$ , and  $21.5 t_{cc}$ . Note the different spatial scale used in the last three panels. The colour scale is  $\log_{10} \rho$ , and spans the range  $-4.5$  (blue) to  $+1.0$  (red).

directions ( $\delta v_r$  and  $\delta v_z$ , respectively), its volume ( $V$ ), its mean density ( $\langle \rho \rangle$ ), and the total circulation produced ( $\Sigma$ ). The whole of the cloud and the densest part of its core are distinguished by the value of the scalar variable  $\kappa$  associated with the cloud (see Pittard et al. 2009). In this way, each global statistic can be computed for the region associated only with the core (identified with the subscript

“core”, e.g.,  $a_{\text{core}}$ ) or with the entire cloud (identified with the subscript “cloud”, e.g.,  $a_{\text{cloud}}$ ).

The characteristic time for the cloud to be crushed by the shocks driven into it is the “cloud crushing” time,  $t_{cc} = \chi^{1/2} r_c / v_b$ , where  $v_b$  is the velocity of the shock in the intercloud (ambient) medium (Klein et al. 1994). Several other timescales are obtained from the simulations. The

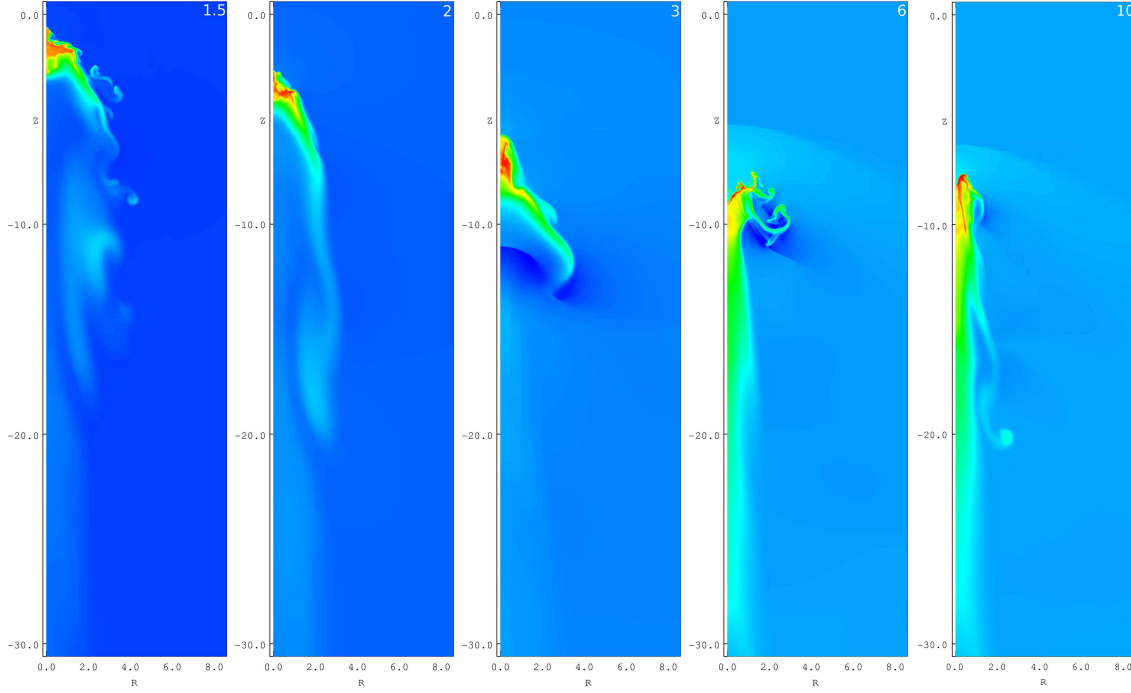


**Figure 2.** Comparison of the mass density distributions at  $t = 5.66 t_{cc}$  for  $k$ - $\epsilon$  subgrid turbulence calculations of  $\chi = 10^3$  clouds hit by adiabatic shocks with Mach numbers of 1.5 (left), 2, 3, 6, and 10 (right). The density colour scale is the same as in Fig. 1.

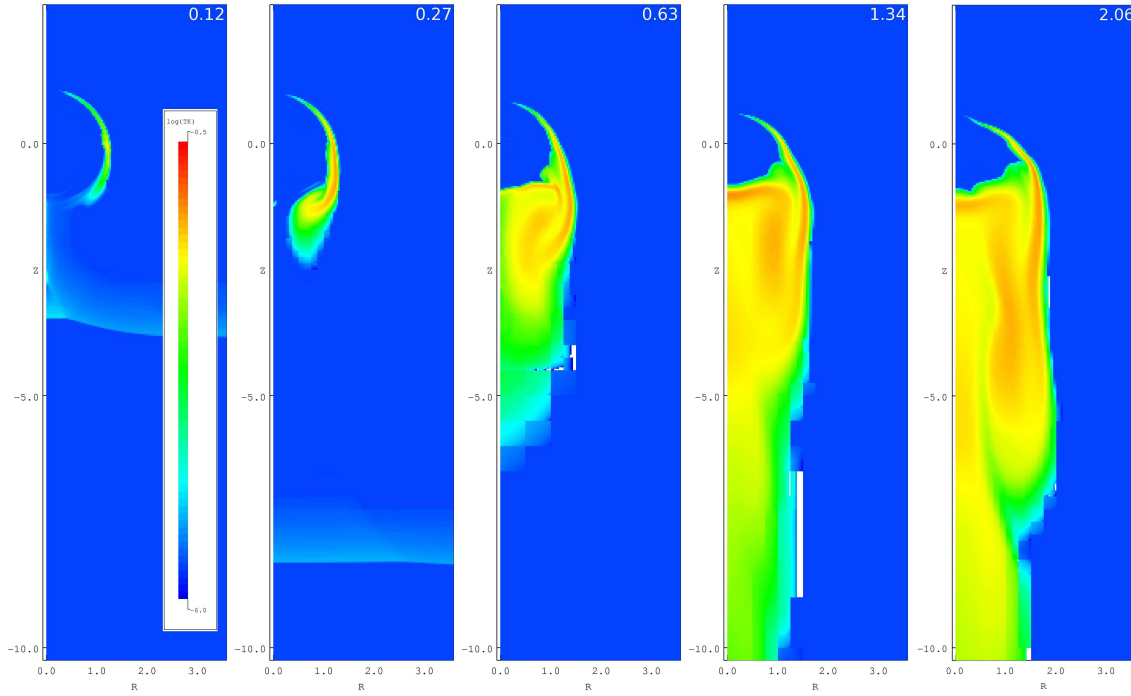


**Figure 3.** Snapshots of the turbulent energy per unit mass,  $k$ , from the  $k$ - $\epsilon$  calculation with  $\chi = 10^3$  and  $M = 1.5$  (model m1.5c3). The evolution proceeds left to right with  $t = 0.12, 0.27, 0.63, 1.34$ , and  $2.06 t_{cc}$ . The white rectangular regions are artefacts of the plotting routine.

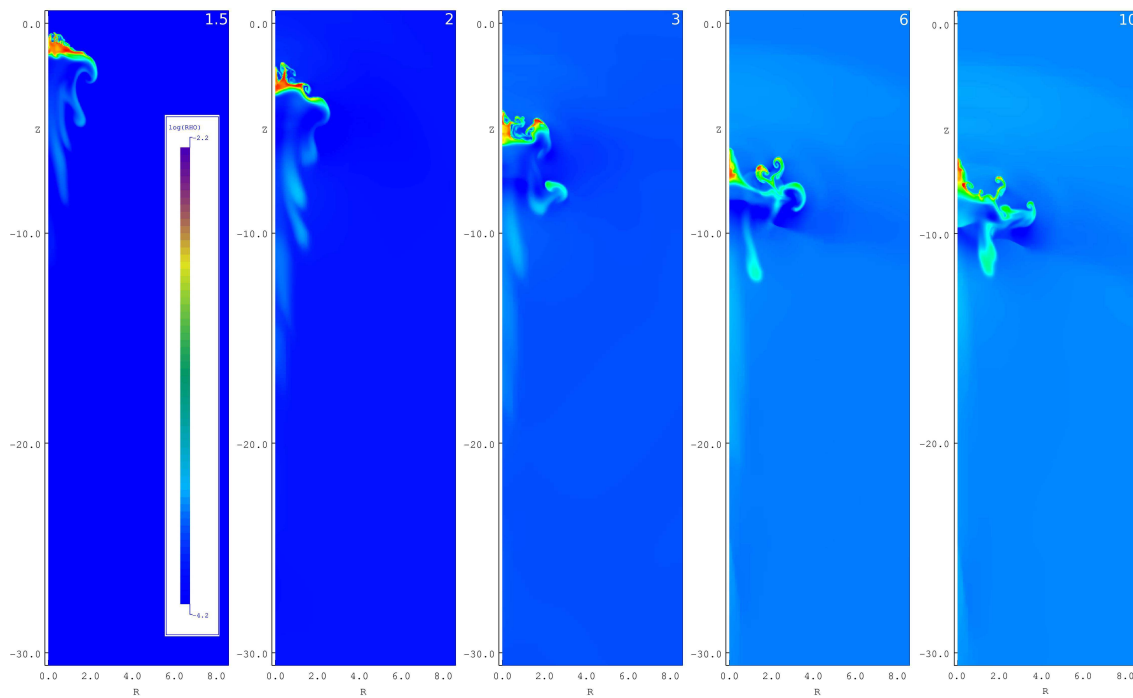


**Figure 4.** Comparison of the mass density distributions from  $k$ - $\epsilon$  subgrid turbulence models at  $t = 4.85 t_{cc}$  for clouds with  $\chi = 10^2$  hit by adiabatic shocks with Mach numbers of 1.5 (left), 2, 3, 6, and 10 (right).

time for the average velocity of the cloud relative to that of the postshock ambient flow to decrease by a factor of  $1/e$  is defined as the “drag time”,  $t_{\text{drag}}$ . The “mixing time”,  $t_{\text{mix}}$ , is defined as the time when the mass of the core of the cloud,  $m_{\text{core}}$ , reaches half of its initial value. The zero-point of all time measurements occurs when the intercloud shock is level with the centre of the cloud.

The diffusive nature of turbulence means that the cloud gradually disperses even when no shock is present. The time needed for the maximum density in the core of a cloud with  $\chi = 10$  to drop to half its original value is  $\approx 150 t_{cc}$ , reducing to  $\approx 4 t_{cc}$  for a cloud with  $\chi = 10^3$ . A comparison of these timescales to the cloud destruction timescales discussed in Section 4 reveals that the evolution of the cloud is always dominated by its interaction with the shock.

### 3 STAGES AND “MACH SCALING”

The main stages of an adiabatic, non-magnetized and non-conducting interaction of a high Mach number shock with a cloud have been described many times in the literature (see, e.g., Klein et al. 1994; Pittard et al. 2009). Initially the cloud is compressed mainly in the  $z$ -direction by the incident shock which propagates into the cloud and by a shock driven into the back of the cloud, and a bow shock propagates upstream into the ambient medium<sup>1</sup>. The over-

pressured cloud then expands downstream and laterally, and Rayleigh-Taylor (RT) and Kelvin-Helmholtz (KH) instabilities destroy the cloud and mix its material into the surrounding flow. The cloud is more rigid, and is better able to resist the passage of the shock, as  $\chi$  increases<sup>2</sup>.

The conditions behind a strong shock are virtually independent of the sound speed ahead of the shock (e.g., for  $M = 10$ , the post-shock density is within a few percent of its value at  $M \rightarrow \infty$ , while the normalized post-shock pressure is within a fraction of a percent). Since the inviscid, adiabatic, non-magnetized and non-conducting hydrodynamic equations are invariant under the transformation

$$t \rightarrow tM, \quad v \rightarrow \frac{v}{M}, \quad P \rightarrow \frac{P}{M^2}, \quad (3)$$

with the position and density unchanged, the time evolution of the cloud is independent of the Mach number of the shock when expressed in units of  $t/t_{cc} \propto tM$  in the limit  $M \rightarrow \infty$ . This is referred to as “Mach scaling”, and was demonstrated to be reasonably valid for clouds with sharp (Klein et al. 1994) and with smooth (Nakamura et al. 2006) boundaries.

The system of equations used for the  $k$ - $\epsilon$  calculations are shown in Pittard et al. (2009). They are invariant under the additional transformation

$$k \rightarrow \frac{k}{M^2}, \quad \epsilon \rightarrow \frac{\epsilon}{M^3}, \quad (4)$$

so Mach scaling occurs in this case also when  $M \rightarrow \infty$ .

<sup>1</sup> The Mach numbers of the reflected and transmitted shocks, in the one-dimensional planar limit, are calculated in Miesch & Zweibel (1994). Unfortunately, in the strong, adiabatic shock limit, the analytical solution for the value of the Mach number of the reflected shock,  $M_r$ , does not satisfy the original

assumption that  $M_r^2 \gg 1$ , and so is known to be quantitatively incorrect. A 6<sup>th</sup>-order polynomial must instead be solved numerically.

<sup>2</sup> In fact, only clouds with  $\chi > 10^3$  should be considered “rigid” (Miesch & Zweibel 1994).



At lower Mach numbers, the post-shock conditions are dependent on the shock Mach number and Mach scaling is not applicable. The evolution of the interaction is also different to the strong-shock case, as shown below.

## 4 RESULTS

In this section we first examine the Mach number dependence of the interaction of a shock with a cloud of high density contrast ( $\chi = 10^3$ ). This extends the work in Pittard et al. (2009) to a range of Mach numbers. The dependence of the interaction on  $\chi$  is then examined, after which we are able to draw some conclusions about the necessary conditions for material stripped from the cloud to form identifiable tails. We then examine three main themes: the Mach scaling of the interaction and the principal differences which result when the post-shock flow is subsonic; the generation of turbulence in the interaction; and the mass-loss rate and the lifetime of the cloud. Some key parameters from the simulations are tabulated in Table 2.

### 4.1 Cloud morphology and turbulence

#### 4.1.1 Interactions with $\chi = 10^3$

Fig. 1 shows snapshots of the density distribution at different times for the case of an adiabatic Mach 1.5 shock impacting a cloud with a density contrast  $\chi = 10^3$ . The interaction is much milder than in the Mach 10 case (see Pittard et al. 2009), which results in several major differences (cf. Nakamura et al. 2006): i) the postshock flow is subsonic with respect to the cloud, so a bowwave rather than a bowshock forms ahead of the cloud; ii) the compression of the cloud is more isotropic; iii) a strong vortex ring is not produced; iv) the smaller velocity difference at the slip surface around the cloud limits the KH and RT instabilities which develop strongly in the  $M = 10$  case; v) it takes much longer for the cloud to be mixed into the surrounding flow and for it to accelerate to the intercloud postshock speed. A comparison with the results from an inviscid code (without the subgrid turbulence model) reveals that the evolution is overall very similar. This was also the case for the Mach 10 interaction studied in Pittard et al. (2009), though significant differences occur if the post-shock medium sweeping over the cloud is very turbulent.

Direct comparison of the density structure at  $t = 5.66 t_{cc}$  for interactions with Mach 1.5, 2, 3, 6 and 10 shocks are made in Fig. 2. There are significant differences between the density distributions from the low Mach number interactions on the one hand, and the high Mach number interactions on the other. At high Mach numbers ( $M > 2.76$ ) the post-shock flow is supersonic, and a bowshock develops around the cloud. The shock driven into the cloud is stronger, and less symmetric. The faster flow speed past the cloud results in faster growth of RT and KH instabilities, and more rapid acceleration of the cloud.

The  $M = 6$  and  $M = 10$  simulations show dense elongated tails at  $t = 5.66 t_{cc}$ , whereas the lower Mach number simulations do not. Since long tails do eventually form even in the Mach 1.5 interaction, it is apparent that material stripped off the cloud forms a longer tail at a given time

(measured in units of  $t_{cc}$ ) as the Mach number increases (the  $M = 3$  simulation forms a long well-defined tail by  $t = 8.54 t_{cc}$ ). This is because the stripping of material is more efficient at higher Mach numbers due to the faster growth of RT and KH instabilities. Fig. 2 also shows that the acceleration of the cloud increases with the Mach number of the interaction, though at very high Mach numbers Mach scaling (Section 3) holds.

The development of turbulence in model m1.5c3 is shown in Fig. 3, where the turbulent energy per unit mass,  $k$ , is displayed.  $k$  is initially created in a thin turbulent boundary layer at the surface of the cloud where a region of high shear exists. The turbulent eddies are then advected by the flow and a turbulent wake develops downstream of the cloud, with a setup time  $\sim t_{cc}$ . This behaviour is qualitatively similar to the Mach 10 case shown in Pittard et al. (2009), although the peak turbulent intensity is smaller, and a supersonic vortex ring and its associated turbulence are not present.

#### 4.1.2 Interactions with $\chi = 10^2$ and $\chi = 10$

Clouds with density contrast  $\chi = 10^2$  are less rigid obstacles to the passage of a shock than clouds with  $\chi = 10^3$ . This can easily be discerned by comparing snapshots of the mass density at  $t = 4.85 t_{cc}$  in interactions of shocks of various Mach numbers with clouds of density contrast  $\chi = 10^2$  as shown in Fig. 4, to the snapshots in Fig. 2 of interactions with  $\chi = 10^3$ .

In fact, Klein et al. (1994) noted that the *nature* of the interaction appears to change with  $\chi$ : at low  $\chi$  the cloud is liable to break up into several large fragments, whereas at large  $\chi$  the core remains more intact and material is stripped from its surface (this is a less effective mixing mechanism). This observation is partially supported by the density snapshots shown in Pittard et al. (2009), where the last panel in each of Figs. 9, 10 and 4 shows snapshots at similar times for a Mach 10 shock interacting with a cloud where  $\chi = 10$ ,  $10^2$ , and  $10^3$ , respectively. However, a closer examination of the statistics of the interaction reveals that in almost all of the cases investigated in this work, the  $\chi = 10^2$  cloud is destroyed faster than clouds with  $\chi = 10$  and  $10^3$  (the exception is the  $M = 1.5$  simulation, where the  $\chi = 10$  cloud is actually destroyed faster). The generally rapid destruction of clouds with  $\chi = 10^2$  appears to be due to the fact that such clouds undergo a more rapid increase in their transverse radius as they expand following the initial compression caused by the passage of the shock (see Fig. 5). This makes the cloud more vulnerable to fragmentation.

The interaction of an adiabatic shock with a cloud of density contrast  $\chi = 10$  has been discussed many times in the literature, which in the interest of brevity we do not repeat here. However, Klein et al. (1994) notes that the axial stretching of the cloud increases with  $\chi$ . This is important insofar as we do not see a well-defined tail in any of our simulations when  $\chi \lesssim 10^2$ . It appears, therefore, that well-defined tails only form in interactions with density contrasts  $\chi \gtrsim 10^3$ , though in such cases they can form across a wide range of Mach numbers.

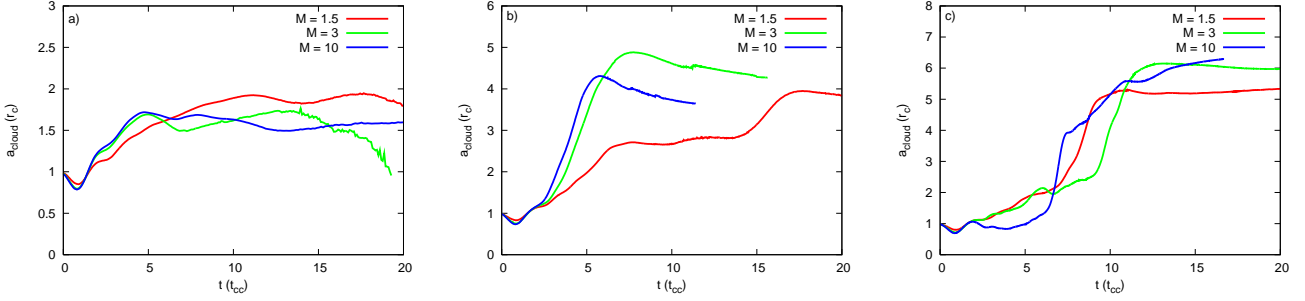


**Figure 5.** Time evolution of the effective transverse radius of the cloud,  $a_{\text{cloud}}$ , for various Mach numbers and density contrasts: (a)  $\chi = 10$ , (b)  $\chi = 10^2$ , (c)  $\chi = 10^3$ .

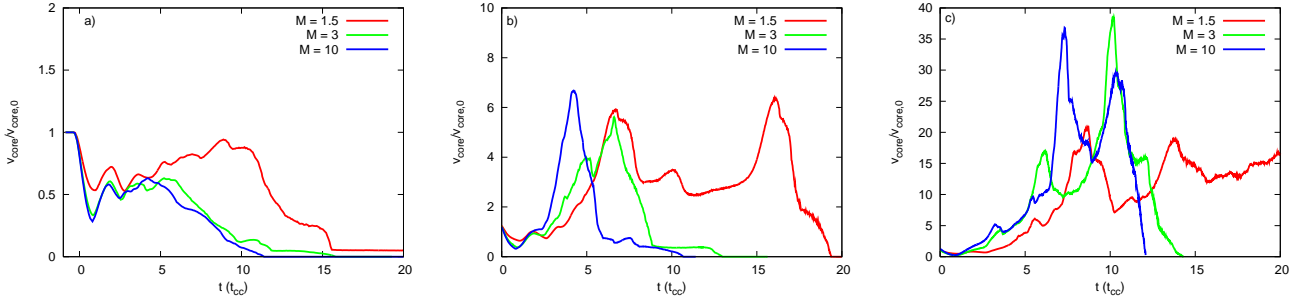


**Figure 6.** Time evolution of the volume of the core of the cloud,  $V_{\text{core}}$ , normalized to its initial value, for various Mach numbers and density contrasts: (a)  $\chi = 10$ , (b)  $\chi = 10^2$ , (c)  $\chi = 10^3$ .

## 4.2 Mach scaling and principle changes for subsonic post-shock flow

In this section we further examine how the interaction changes with the Mach number, and the major differences which occur when the post-shock flow is subsonic.

### 4.2.1 Cloud shape, volume, and mean density

Fig. 5 shows that the initial compression of the cloud in the transverse direction is weakest in the  $M = 1.5$  simulation, but comparable in the  $M = 3$  and  $M = 10$  simulations. The transverse expansion which follows as the cloud seeks to re-establish pressure equilibrium is typically slower in the  $M = 1.5$  simulations, but occurs at a similar rate in the  $M = 3$  and  $M = 10$  simulations.

That the initial compression of the cloud is weaker at low Mach numbers can also be discerned from Fig. 6(a). For low density contrasts ( $\chi \lesssim 10$ ) the core of the cloud maintains a larger volume than when hit by a stronger shock. However, clouds with higher density contrast hit by a strong shock undergo a violent re-expansion after their initial compression, causing their core volume to exceed their counterparts hit by weaker shocks (see panels (b) and (c) in Fig. 6). At later times the volume of the cloud core decreases as the core material is gradually ablated and mixed into the surrounding flow.

The reduced compressions behind low Mach number shocks relative to their stronger counterparts cause lower peak densities of the clouds and their core material,  $\langle \rho_{\text{cloud}} \rangle / \rho_{\text{max}}$  and  $\langle \rho_{\text{core}} \rangle / \rho_{\text{max}}$ , respectively (see Fig. 7). And although the decline in these quantities over the period  $t \lesssim 5 t_{\text{cc}}$  is slower in the Mach 1.5 simulations, due to the

slower stripping of material into the flow, the final value of  $\langle \rho_{\text{cloud}} \rangle / \rho_{\text{max}}$  that is reached is lower in the Mach 1.5 simulations than in the higher Mach number simulations, since the density of the postshock ambient material is lower in this case. This is particularly noticeable in Fig. 7(a).

### 4.2.2 Cloud velocity

At lower Mach numbers there is a gentler acceleration of the cloud and its core in the axial direction, shown by the mean velocity statistics,  $\langle v_{z,\text{cloud}} \rangle$  and  $\langle v_{z,\text{core}} \rangle$ , respectively (panels (a-c) and (d-e) in Fig. 8). This reflects both the weaker shock that is initially driven into the cloud, and the slower speed of the post-shock flow past the cloud. The acceleration of the cloud to a velocity of  $1/e$  times the ambient postshock flow speed is discussed further in Section 4.2.6.

### 4.2.3 Cloud mass

The slower post-shock flow in the simulations with lower Mach numbers affects the growth rate of RT and KH instabilities. This in turn affects the speed at which material is ripped from the surface of the cloud and the time for the cloud to mix into the flow. Hence,  $m_{\text{core}}$  declines more rapidly in simulations with higher Mach numbers (see Fig. 9). In high Mach number interactions the core completely disappears shortly after  $t_{\text{mix}}$ , whereas at lower Mach numbers material may be identified as originating from the core for times considerably after  $t_{\text{mix}}$ . Also of note is that the slope of  $m_{\text{core}}$  in the  $M = 1.5$  simulations appears to get shallower with increasing  $\chi$  (Fig. 9). The maximum slopes of the  $M = 3$  and  $M = 10$  models are particularly steep when



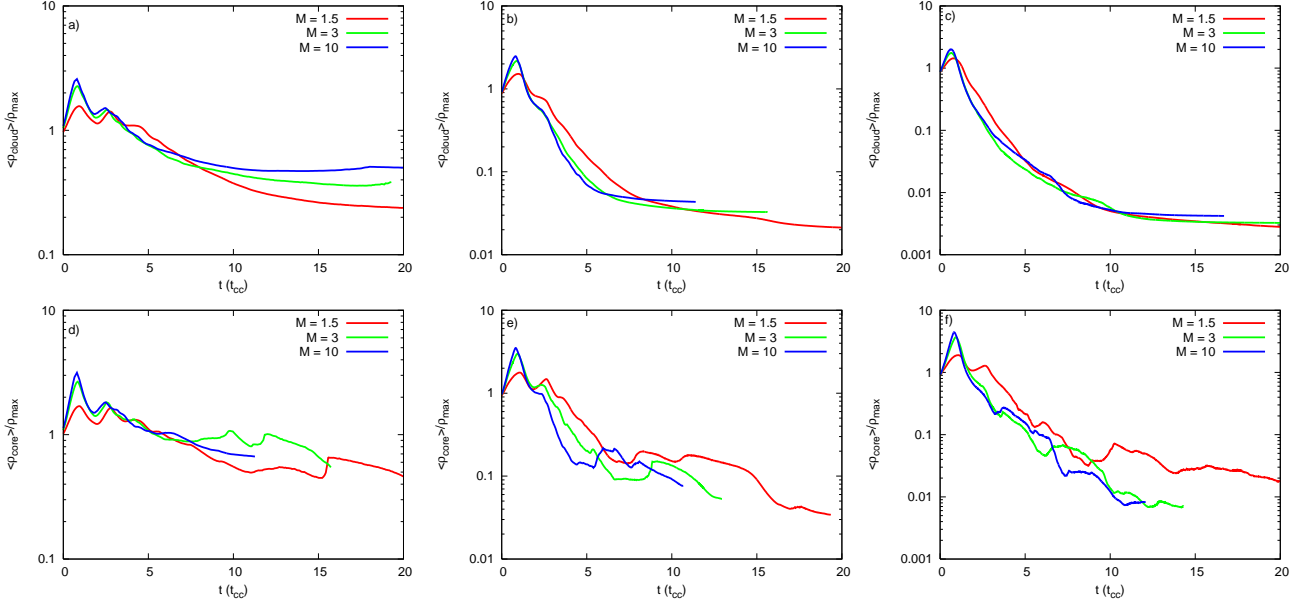


**Figure 7.** Top panels: Time evolution of the mean density of the cloud,  $\langle \rho_{\text{cloud}} \rangle$ , normalized to the initial maximum cloud density, for various Mach numbers and density contrasts: (a)  $\chi = 10$ , (b)  $\chi = 10^2$ , (c)  $\chi = 10^3$ . Bottom panels: As top, but for the mean density of the core,  $\langle \rho_{\text{core}} \rangle$ .

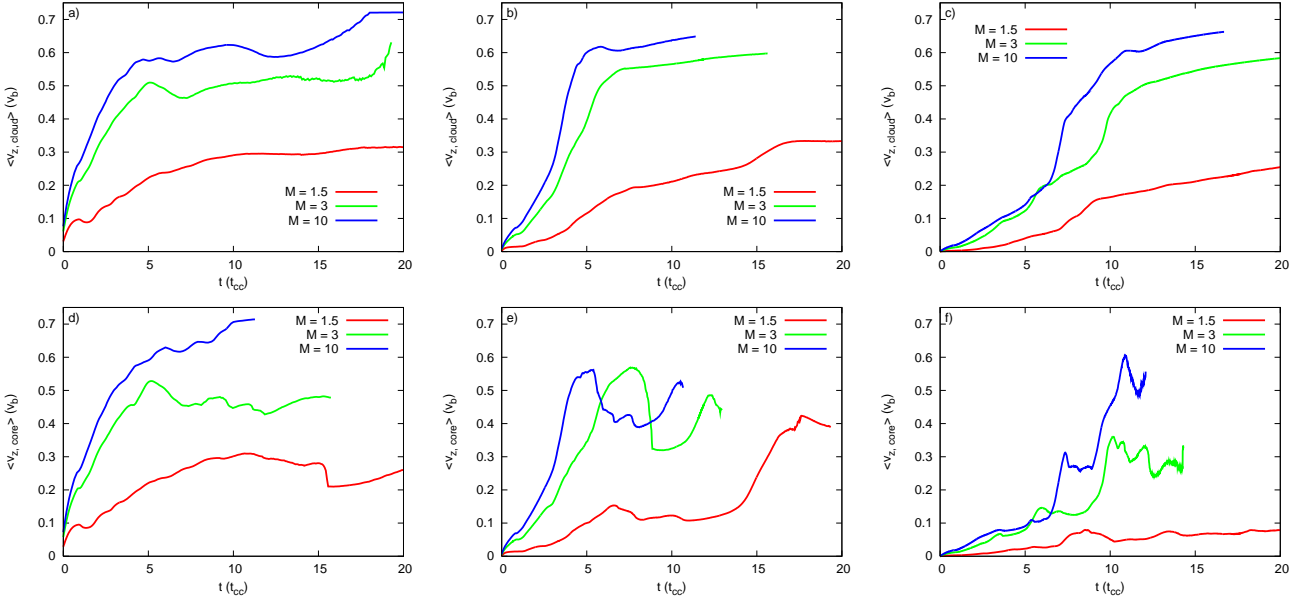


**Figure 8.** Top panels: Time evolution of the cloud mean velocity,  $\langle v_z \rangle_{\text{cloud}}$ , for various Mach numbers and density contrasts: (a)  $\chi = 10$ , (b)  $\chi = 10^2$ , (c)  $\chi = 10^3$ . Bottom panels: as the top panels, but for the core mean velocity,  $\langle v_z \rangle_{\text{core}}$ .

$\chi = 10^2$ , which is likely related to the rapid transverse expansion of the cloud radius, and subsequent strong mixing, taking place in these models (see Section 4.1.2).

The evolution of the cloud and the way that its material mixes with the surrounding gas can also be studied via its mass distribution in density or velocity space. Figs. 10 and 11 show this evolution for clouds with  $\chi = 10^3$ . Fig. 10 shows the fraction of cloud mass over a range of density bins of width  $0.1 \rho_{\text{max}}$ . The first subfigure is shown for  $t = 1.34 t_{\text{cc}}$ , when the transmitted shock has swept through the entire cloud (see, e.g., Fig. 1). In the  $M = 1.5$  simu-

lation, the weak shock transmitted into the cloud initially compresses the gas by a factor of 1.7. Slightly higher values are subsequently obtained as the shock converges on the cloud centre. In contrast, the stronger shocks in the  $M = 3$  and  $M = 10$  simulations produce higher compressions which can exceed a factor of 10 (see Fig. 19 in Pittard et al. 2009). At later times the density of the cloud material drops slowly towards the ambient post-shock density as the cloud continues to expand into and mix with the surrounding gas.

Fig. 10 also reveals that flatter mass distributions are obtained during higher Mach number interactions, whereas

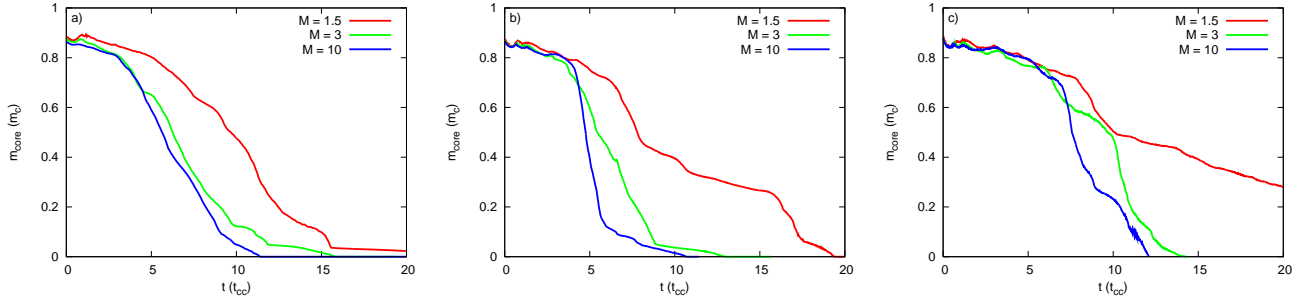


**Figure 9.** Time evolution of the core mass,  $m_{\text{core}}$ , for various Mach numbers and density contrasts: (a)  $\chi = 10$ , (b)  $\chi = 10^2$ , (c)  $\chi = 10^3$ .

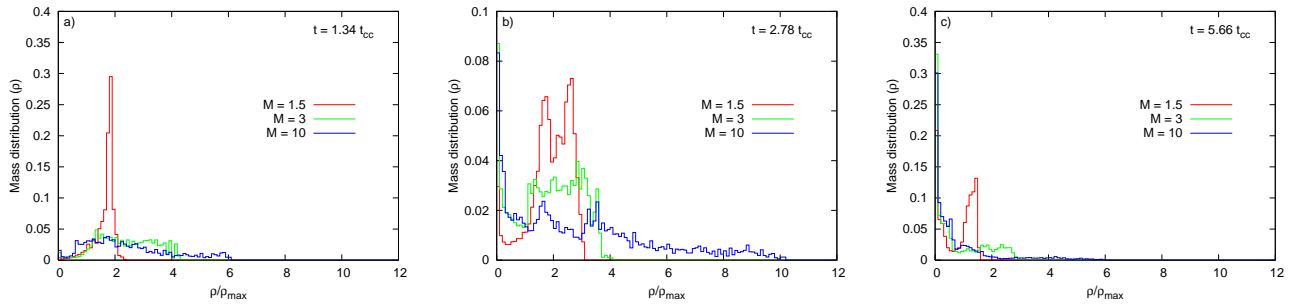


**Figure 10.** Time evolution of the mass density distributions for models with  $\chi = 10^3$  and varying shock Mach numbers. The histograms indicate the cloud mass contained within each density bin of width  $0.1\rho_{\text{max}}$ , normalized to the total cloud mass,  $m_c$ . From left to right the mass fractions were computed at  $t = 1.34, 2.78$  and  $5.66 t_{\text{cc}}$ .

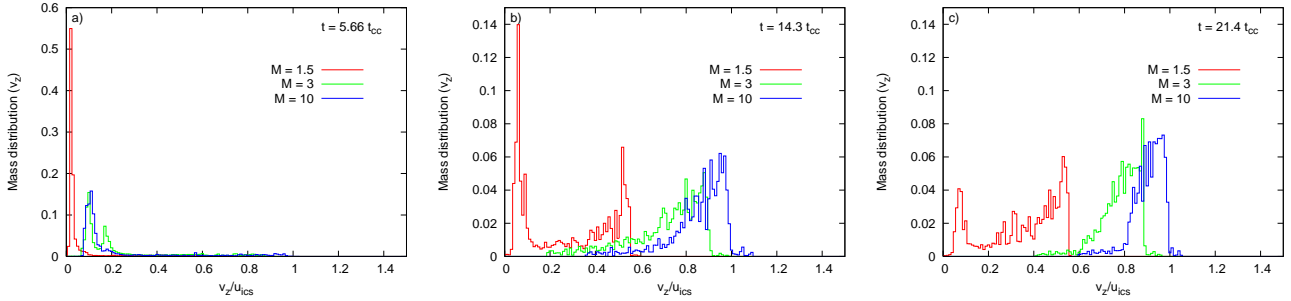


**Figure 11.** Mass distributions as a function of  $v_z$  (normalized to the post-shock velocity in the ambient medium,  $u_{\text{ics}}$ ) for models with  $\chi = 10^3$  and varying shock Mach numbers at  $t = 5.66, 14.3$  and  $21.4 t_{\text{cc}}$ . The histograms denote the mass contained within a velocity bin of width  $0.01 u_{\text{ics}}$  for a line of sight parallel to the  $z$ -axis. The integrated mass is the mass of the cloud,  $m_c$ .

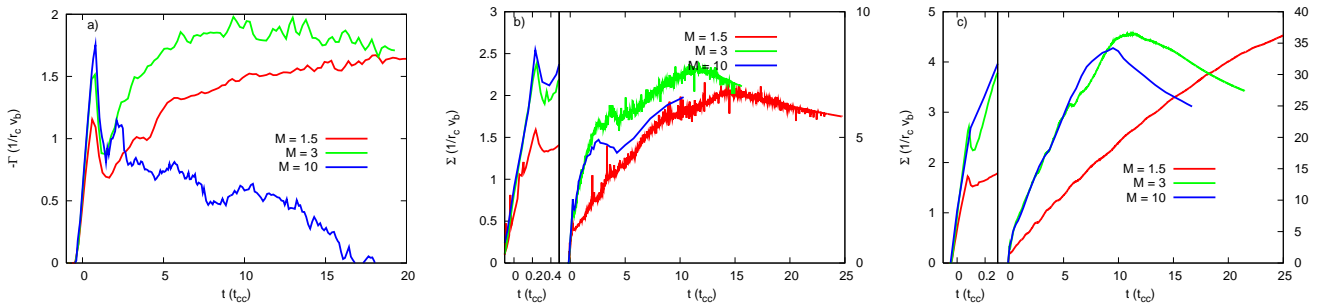


**Figure 12.** Time evolution of the circulation,  $\Gamma_{\text{circ}}$ , for various Mach numbers and density contrasts: (a)  $\chi = 10$ , (b)  $\chi = 10^2$ , (c)  $\chi = 10^3$ .

the distribution is more concentrated and peaky in simulations with lower Mach numbers. Two distinct clusters of mass at densities above and below  $2 \rho_{\max}$  can be seen in the  $M = 1.5$  simulation at  $t = 2.78 t_{cc}$ . This is not just a consequence of the higher Mach number cases being more evolved - the mass distribution in the  $M = 1.5$  simulation never approaches the flatness seen in the higher Mach number cases, even at much later times.

The flatter mass distribution in the high Mach number cases reflects differences in the dynamical state of the cloud core with the Mach number of the interaction. At  $t \approx 1.34 t_{cc}$ , the cloud hit by the Mach 10 shock is violently re-expanding (see Fig. 4 of Pittard et al. 2009). This expansion is supersonic, which leads to a relatively low density in the central region of the cloud, with higher densities in the shocked region around the periphery of the cloud. At  $t \approx 2.78 t_{cc}$ , the cloud core is relatively dispersed, with fingers of somewhat lower density material around its edges. Therefore, at both of these instances, the density of material in the core of the cloud spans a wide range. In contrast, in the Mach 1.5 case, Fig. 1 shows that at  $t = 1.34 t_{cc}$ , the core density of the cloud is approximately constant. Since the interaction is much milder, the gentler rebounding of the cloud in the Mach 1.5 case does not lead to such a wide range of densities, and therefore a more concentrated and peaky distribution is obtained as seen in Fig. 10.

Fig. 11 shows the mass distribution function in velocity space within the entire cloud integrated along the  $z$ -axis. The histograms indicate the fraction of the cloud mass contained within a velocity bin of width  $0.01 u_{ics}$ , where  $u_{ics}$  is the post-shock velocity of the ambient medium. Initially the cloud is at rest, and its velocity is zero. When the material within the cloud is fully mixed into the surrounding flow its velocity is equal to  $u_{ics}$  (a small fraction of mass exceeds this value due to turbulent motions). The slower acceleration of material in the  $M = 1.5$  simulation is again clearly evident.

#### 4.2.4 Circulation

A central aspect of the interaction of a shock with a cloud is the development of vorticity,  $\omega$ , and circulation,  $\Gamma$  (see Klein et al. 1994). Production of the latter can be divided into three main components: at the interface between the cloud and the surrounding flow by the initial passage of the shock ( $\Gamma_{\text{shock}}$ ) and the subsequent postshock flow ( $\Gamma_{\text{post}}$ ), and at the triple points associated with the Mach-reflected shocks behind the cloud ( $\Gamma_{\text{ring}}$ ). For the general case of a shock of Mach number  $M$  and a ratio of specific heats  $\gamma$ , these components are:

$$\Gamma_{\text{shock}} \approx -\frac{6}{\gamma+1} \left( \frac{M^2-1}{M^2} \right) \left( 1 - \frac{1}{\chi^{1/2}} \right) v_b r_c, \quad (5)$$

$$\Gamma_{\text{post}} \approx -\frac{1}{(\gamma+1)^2} \left( \frac{M^2-1}{M^2} \right)^2 \left( \frac{\chi^{1/2} t_{\text{drag}}}{t_{cc}} \right) v_b r_c, \quad (6)$$

$$\Gamma_{\text{ring}} \approx \frac{2}{\gamma+1} \left( \frac{M^2-1}{M^2} \right) v_b r_c. \quad (7)$$

Note that the circulation generated by the vortex ring is positive, while the passage of the shock and the postshock flow generates negative circulation.

The contribution of these three components to the to-

**Table 3.** Analytical estimates for the total circulation and its various components produced by the postshock flow. In each case the calculation of the value uses the drag-time for the core as given in Table 2.  $\Gamma_{\text{ring}} = 0.417, 0.667$ , and  $0.743$  when  $M = 1.5, 3$  and  $10$ , respectively. In the fifth column the numerically determined peak values of the total circulation,  $-\Gamma_{\text{tot}})_p$ , are given, while the sixth column notes the dominant component(s).

Model	$-\Gamma_{\text{shock}}$	$-\Gamma_{\text{post}}$	$-\Gamma_{\text{tot}}$	$-\Gamma_{\text{tot}})_p$	Dom. comp.
m1.5c1	0.85	0.42	0.84	1.60	$\Gamma_{\text{shock}}$ and $\Gamma_{\text{post}}$
m3c1	1.37	0.52	1.22	1.95	$\Gamma_{\text{shock}}$ and $\Gamma_{\text{post}}$
m10c1	1.52	0.48	1.26	1.75	$\Gamma_{\text{shock}}$
m1.5c2	1.12	6.06	6.76	6.76	$\Gamma_{\text{post}}$
m3c2	1.80	4.20	5.33	7.48	$\Gamma_{\text{post}}$
m10c2	2.00	4.26	5.52	6.60*	$\Gamma_{\text{post}}$
m1.5c3	1.20	40.7	41.5	37.2	$\Gamma_{\text{post}}$
m3c3	1.94	34.2	35.4	36.5	$\Gamma_{\text{post}}$
m10c3	2.15	31.2	32.6	34.2	$\Gamma_{\text{post}}$

Note: (\*) The absolute value of the total circulation in model m10c2 was still rising at the time the simulation was stopped.

tal circulation can be seen in Fig. 12(a). The passage of the shock over the cloud causes the initial rise to maximum ( $\Gamma_{\text{shock}}$ ), with the formation of the vortex ring behind the cloud ( $\Gamma_{\text{ring}}$ ) causing the subsequent drop. The post-shock flow past the cloud generates further vorticity which increases the circulation after this minimum ( $\Gamma_{\text{post}}$ ). Figs. 12(b) and (c) demonstrate the increasing dominance of  $\Gamma_{\text{post}}$  with increasing  $\chi$ .

The predicted total circulation agrees better with the numerical results when the core (rather than the cloud) value is used for  $t_{\text{drag}}$  in Eq. 6 (as also found by Pittard et al. 2009). Table 3 shows the predicted and measured values.

#### 4.2.5 Energy evolution

Figs. 13 and 14 show the gain in kinetic and thermal energy of the cloud material, and the growth (and subsequent decay) of turbulent energy for simulations as a function of Mach number and cloud density contrast. The cloud material should eventually acquire the same kinetic and thermal energy density as the ambient medium, and the turbulent energy should dissipate as heat. The ratio of kinetic to thermal energy in the postshock flow of an adiabatic shock is  $E_k/E_{\text{th}} = \gamma M_{\text{ps}}^2/3$ , where  $M_{\text{ps}}$  is the postshock Mach number measured in the frame of the undisturbed, upstream, ambient medium. It can be easily shown that

$$M_{\text{ps}} = \frac{2(M^2-1)}{\sqrt{[2\gamma M^2 - (\gamma-1)][(\gamma-1)M^2 + 2]}}. \quad (8)$$

Since  $M_{\text{ps}} = 0.511, 1.044$  and  $1.310$  for  $M = 1.5, M = 3$ , and  $M = 10$  shocks, at late times we expect that  $E_k/E_{\text{th}} = 0.145, 0.607$ , and  $0.954$  respectively. Note that  $E_k/E_{\text{th}} = 1.0$  in the strong shock ( $M \rightarrow \infty$ ) limit.

The plots of the kinetic energies of the cloud material in Fig. 13 are normalized against the values which the cloud material should eventually obtain once it fully mixes into, and becomes indistinguishable from, the post-shock flow. As can be seen, the timescales for this can be very long,

especially when the Mach number of the shock is low and the cloud density contrast is high (when  $M = 1.5$  and  $\chi = 10^3$ , the cloud material has attained less than 60 per cent of its fully-mixed kinetic energy at  $t = 25 t_{cc}$ ).

Fig. 13 shows that the cloud's rate of gain of kinetic energy at a given value of  $\chi$  is similar in the  $M = 3$  and  $M = 10$  models, and in comparison is considerably slower in the  $M = 1.5$  models. The same behaviour is seen for the thermal energy. In shock-cloud interactions with  $M = 1.5$  the rate of energy gain is very gradual and almost linear in time. In contrast, when  $M \geq 3$ , there is rapid transfer of kinetic energy to clouds with  $\chi = 10$ , with a much slower transfer of thermal energy such that  $E_k/E_{th}$  can be significantly greater than unity over a substantial time period, before finally dropping back below unity as it approaches its asymptotic limit. The transfer of kinetic energy to clouds with  $\chi = 10^2$  and  $10^3$  shows a noticeable and relatively short-lived increase in its rate when  $t \sim t_{drag}$  for the cloud (this is also when  $t \sim t_{mix}$ ), after which it slows. Fig. 14 shows that the cloud's rate of gain of kinetic and thermal energy at a given Mach number is initially much more rapid for lower values of  $\chi$ .

The evolution of the turbulent energy is discussed in Section 4.3.

#### 4.2.6 $t_{drag}$ and $t_{mix}$

Fig. 15 shows the Mach number and  $\chi$  dependence of  $t_{drag}$  and  $t_{mix}$ , two of the important timescales which characterize the evolution and destruction of the cloud. The results of least-squares fits to these plots are noted in Tables 4 and 5. Both  $t_{drag}$  and  $t_{mix}$  are relatively constant for a given  $\chi$  at Mach numbers above 4. This reflects the onset of the ‘‘Mach-scaling’’ mentioned in Section 3. In contrast,  $t_{drag}$  and  $t_{mix}$  both rise sharply at lower Mach numbers: cloud drag and the mixing of material from the cloud are less efficient with low shock Mach numbers. This is because: i) the density jump across the shock and the speed of the postshock intercloud flow past the cloud are lower when  $M$  is smaller; and ii) the growth rate of KH instabilities is slower.

The cloud is accelerated by two processes. First, the shock driven into the cloud accelerates it to a speed  $v_s$ . Further acceleration then occurs as the shocked intercloud gas flows past the cloud, until they have the same velocity. For large  $\chi$  the second stage dominates and  $v_s/v_b$  is small. Solving the equation of motion for the cloud (see, e.g., Eq. 2.5 in Klein et al. 1994) in the strong shock limit for  $\gamma = 5/3$  gives

$$t_{drag(s)} = 1.53 \frac{\chi^{1/2}}{C_D} t_{cc}, \quad (9)$$

where  $C_D$  is the drag coefficient (see Section 2.1 of Klein et al. 1994). In the general case we find

$$t_{drag(g)} = 2.3 \frac{(\gamma - 1)M^2 + 2}{(M^2 - 1)} \frac{\chi^{1/2}}{C_D} t_{cc}. \quad (10)$$

For both Eqs. 9 and 10, the cross-sectional area of the cloud is assumed to remain constant. This is a poor approximation which leads to an overestimate of the drag time, since the shock causes the cloud to rapidly expand in the transverse direction (Fig. 5). Nonetheless, it is useful to compare the ratio  $t_{drag(g)}/t_{drag(s)}$  with  $M$ . For  $\gamma = 5/3$  and  $M = 1.5$ , we

find that  $t_{drag(g)}/t_{drag(s)} \approx 4$ . Comparing to Fig. 15(a) we see that the ratio of  $t_{drag}$  when  $M = 1.5$  to when  $M = 40$  is 3.3, 2.0, and 1.7 for  $\chi = 10$ ,  $10^2$ , and  $10^3$ , respectively. Hence the Mach number dependence of the drag time scales nearly as expected when  $\chi = 10$ . However, the drag time for low values of  $M$  is increasingly overestimated compared to the simulations as  $\chi$  increases. This divergence is at least partly due to differences in the expansion behaviour of the cloud: comparing simulations m1.5c3 and m10c3, one sees that  $a_{cloud}$  is significantly greater in the former until  $t \approx 7 t_{cc}$  (see Fig. 5c).

At face value the fits in Fig. 15(a) to the numerically obtained drag times imply that  $C_D \approx 5$ , 5, and 10 for  $\chi = 10$ ,  $10^2$ , and  $10^3$  respectively. These values are much larger than one expects (the true values of  $C_D$  are likely to be  $\lesssim 1$  - see Landau & Lifshitz 1959, for solid bodies). This difference is again caused by the fact that the cross-sectional area of the cloud does not remain constant.

Prior to the Klein et al. (1994) paper, the naive expectation was that the mixing time of the cloud would be comparable to the time taken for the cloud to sweep up a column of postshock material of similar mass to the cloud. However, Klein et al. (1994) discovered that this was not consistent with their results, since there was no evidence for the mixing time scaling as  $\chi^{1/2} t_{cc}$ , and proposed instead that the relevant time was the timescale for KH instabilities to fragment the cloud. The KH growth time is

$$t_{KH} \sim \left( \frac{v_b}{v_{rel}} \right) \frac{1}{k_\lambda r_c} t_{cc}, \quad (11)$$

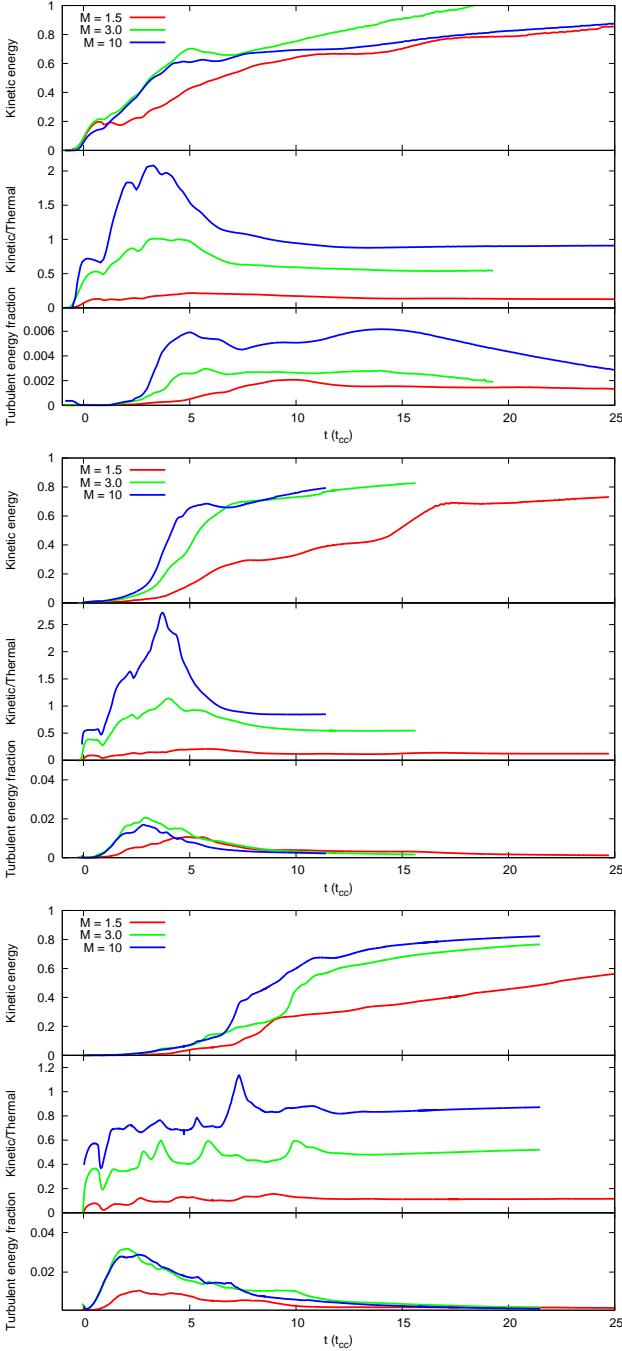
where  $k_\lambda$  is the wavenumber of the perturbation. Longer wavelengths ( $k_\lambda r_c \sim 1$ ) are the most disruptive. Assuming that the relative speed between the postshock flow and the cloud is the post-shock flow speed (i.e. that the cloud is initially stationary after passage of the shock), then  $v_{rel}/v_b = (1 - \rho_0/\rho_s)$ , where  $\rho_0$  and  $\rho_s$  are the preshock and postshock densities of the ambient medium, respectively. Setting  $k_\lambda r_c = 1$ , one then obtains

$$t_{KH} \sim \frac{(\gamma + 1)M^2}{(2M^2 - 2)} t_{cc}. \quad (12)$$

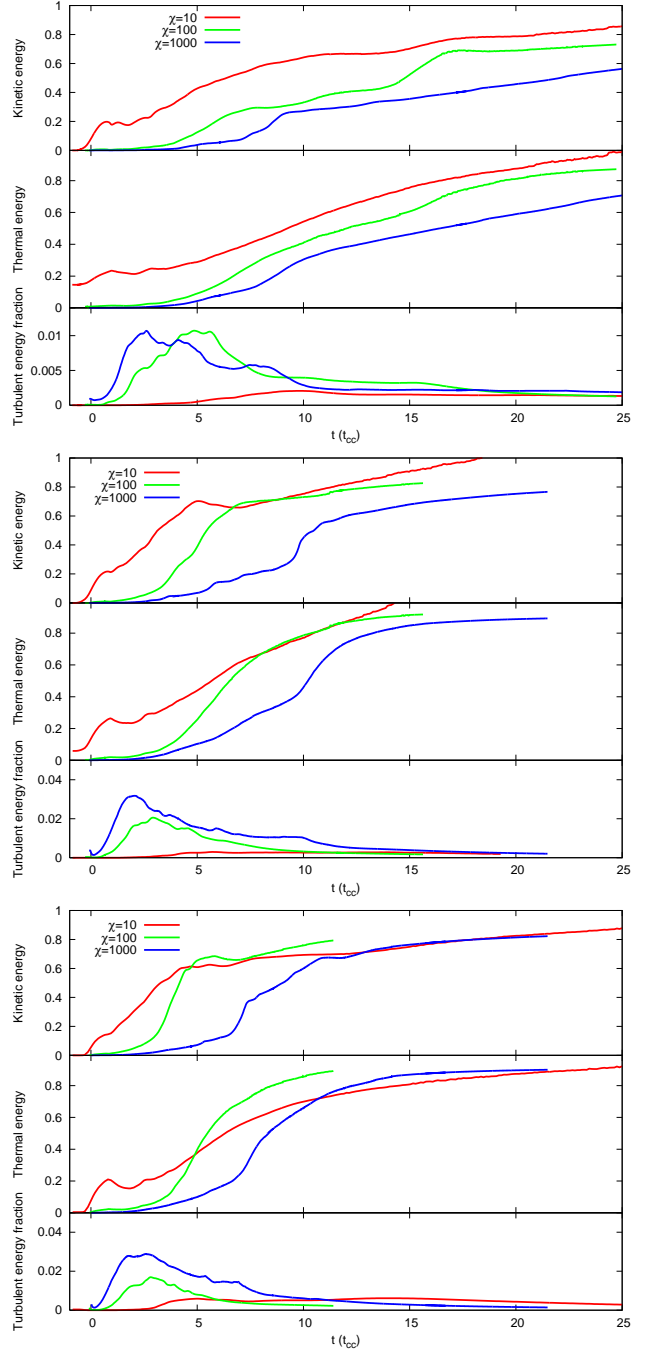
While setting  $t_{mix} = t_{KH}$  does not give the correct magnitude for  $t_{mix}$  (cf. Fig. 15), the relative change with  $M$  (a factor of 1.8 between  $M = 40$  and  $M = 1.5$ ) is close to what is observed in our numerical model.

Fig. 15 also shows that the mixing time of the core,  $t_{mix}$ , is always greater than the drag time of the cloud,  $t_{drag}$ . The ratio of  $t_{mix}/t_{drag}$  is also dependent on  $\chi$ , this ratio being greatest at low values of  $\chi$ , but declining with increasing  $\chi$  as the relative efficiency of mixing relative to acceleration increases. For clouds with  $\chi = 10$ , the numerical simulations reveal that  $t_{mix}/t_{drag}$  increases from 1.39 at  $M = 1.5$ , peaking at 1.67 at  $M = 3$ , and thereafter declines to 1.56 at  $M = 40$ . When  $\chi = 10^3$ ,  $t_{mix}/t_{drag}$  declines from a value of 1.45 at  $M = 1.5$ , to 1.15 at  $M = 40$ .

The values of  $t_{drag}$  and  $t_{mix}$  display greater scatter about the least squares fit when  $\chi = 10^3$  compared to the fits at lower values of  $\chi$ . This is due to large scale RT instabilities in these models which randomly and spontaneously fragment the cloud. The values of  $t_{drag}$  and  $t_{mix}$  are generally higher in inviscid calculations, and display larger scatter. The extra viscosity that the subgrid turbulence model im-



**Figure 13.** The evolution of the cloud kinetic energy (normalized to its asymptotic value once the cloud is fully mixed into the post-shock flow) in models with  $\chi = 10$  (top),  $10^2$  (middle), and  $10^3$  (bottom). The ratio of the cloud’s kinetic to thermal energy and its turbulent energy at *subgrid* scales as a fraction of the total cloud energy at any instant are also shown.



**Figure 14.** As Fig. 13 but each panel is for models with the same shock Mach number:  $M = 1.5$  (top),  $M = 3$  (middle), and  $M = 10$  (bottom). The central plot of each panel now directly shows the thermal energy of cloud material. Note that the scale for the turbulent energy in the top panel differs from that in Fig. 13.

### 4.3 Turbulence in shock-cloud interactions

poses on the hydrodynamic grid helps suppress some of the random fluctuations during the interaction, and also leads to better convergence in resolution tests (Pittard et al. 2009).

The interaction of shocks with clouds is likely to be a key mechanism for generating turbulence in the ISM, since substantial vorticity and velocity dispersion is produced. Turbulent motions in our simulations can be identified on two separate scales: the subgrid turbulence model deals with turbulent motions and mixing on scales smaller than the size



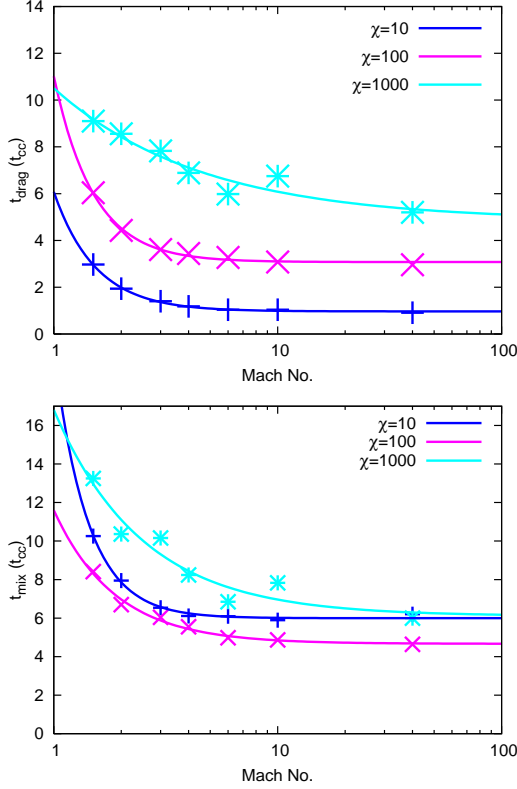


**Figure 15.** Top:  $t_{\text{drag}}$  (for the cloud) and bottom:  $t_{\text{mix}}$  (for the core) as a function of Mach number and  $\chi$  measured from the  $k$ - $\epsilon$  numerical simulations.

of a grid cell, while larger scale (resolved) turbulent motions can be directly measured from the velocity dispersions in the axial and radial directions,  $\delta v_z$  and  $\delta v_r$ , respectively.

#### 4.3.1 The cloud velocity dispersion

Fig. 16 shows the time evolution of the velocity dispersions,  $\delta v_z$  and  $\delta v_r$ . Their behaviours are broadly similar for interactions with supersonic post-shock flow ( $M = 3$  and  $M = 10$ ). However, the velocity dispersions in the  $M = 1.5$  simulations build more slowly, and are limited to lower maximum values, reflecting the weaker interaction.  $\delta v_z$  peaks at higher values with  $\chi$ , due to greater growth of KH and RT instabilities resulting from the longer drag and mixing timescales with  $\chi$ . The ratio  $\delta v_z / \delta v_r$  is not strongly dependent on  $M$ , in contrast to its variation with  $\chi$ . The latter point was noted previously by Klein et al. (1994) and Pittard et al. (2009).

#### 4.3.2 The subgrid turbulent energy

The time evolution of the energy in sub-grid turbulent motions is shown in Fig. 13. It rises more rapidly and peaks at higher values in simulations with high Mach numbers and cloud density contrast. When  $\chi = 10^3$ , it peaks at about 3 percent in models with  $M = 3$  and  $M = 10$ , but peaks at only 1 percent when  $M = 1.5$ . In models with  $\chi = 10$  it peaks at less than 1 per cent, and reaches a maximum value of only 0.2 percent when  $M = 1.5$ . The peak in the sub-grid turbulent energy fraction is relatively narrow when

$\chi \gtrsim 10^2$ , with most of the turbulent energy being dissipated by  $t = 10 t_{\text{cc}}$ . In contrast, when  $\chi = 10$ , the sub-grid turbulent energy can be roughly constant for durations in excess of  $15 t_{\text{cc}}$ .

#### 4.3.3 Locally averaged velocity dispersions

The velocity dispersions shown in Fig. 16 are global averages over the entire cloud. These can be used to obtain a globally averaged energy fraction of the fluctuations. For model m10c3,  $\delta v_r$  and  $\delta v_z$  peak at  $t \approx 7.25 t_{\text{cc}}$ , with values of  $\approx 0.09 v_b$  and  $\approx 0.23 v_b$  respectively. Hence, the global velocity dispersion,  $\delta v = \sqrt{(2\delta v_r^2 + \delta v_z^2)/3} \approx 0.15 v_b$ . This is about twice the value noted by Nakamura et al. (2006) for their simulations of radiative clouds with  $\gamma = 1.1$ . The ratio of the energy in (resolved) fluctuations to the kinetic energy of the mean flow is  $(\delta v/v)^2 \approx 0.2$ .

However, such global estimates of  $\delta v$  and  $(\delta v/v)^2$  are actually upper limits. Fig. 17 shows the mean axial velocity,  $v_z$ , and the velocity dispersions  $\delta v_z$  and  $\delta v_r$ , evaluated on a more local scale. The tiles in these maps are of size  $0.5 \times 0.5 r_c$ , and contain up to 4096 individual cells from the hydrodynamic calculation, over which the displayed quantities are averaged. These averages are again mass-weighted quantities, but consider material only within each tile - i.e.  $\delta v_z$  is again calculated using Eq. 23 in Paper I, but  $\langle v_z^2 \rangle$  and  $\langle v_z \rangle$  are evaluated only for the material within each tile. Note that  $\delta v_r$  will be non-zero even when  $v_r$  is constant over each tile. This is a consequence of the specific averaging formula. The maps in Fig. 17 were calculated at  $t = 5.66 t_{\text{cc}}$  for clouds with  $\chi = 10^3$  hit by a Mach 1.5 (a) and a Mach 10 (b) shock (for which the corresponding density plots are shown in Fig. 2), and also at  $t = 7.10 t_{\text{cc}}$  for the  $M = 10$  case (panel c).

In Fig. 17(a) and (b), the mean axial velocity is highest at the slip surface between cloud and ambient material, and is lowest in the central core of the tail. A velocity gradient perpendicular to the tail is clearly present. Both the  $r$  and  $z$ -components of the velocity dispersion are also greatest at the slip surface. Also shown is  $\log_{10}(\delta v/v)^2$ , which has a maximum value of  $-0.1$  in Fig. 17(a), and  $-0.92$  in Fig. 17(b). Slightly later in the m10c3 simulation, a large fragment breaks away from the cloud core. This fragment is responsible for a significant increase in the local and globally averaged velocity dispersions, as seen in Figs. 17(c) and 16, respectively. The peak local value of  $(\delta v/v)^2 = 0.6$ , indicating that there are regions in the flow where the swirling motions within the gas are almost as fast as its average bulk speed.

Our aim in this section is simply to highlight how the velocity dispersion varies on smaller scales in the flow. This is of interest given that spatial variations in the velocity and the velocity dispersion of clouds and tails can be probed using high-spatial-resolution observations (see, e.g., Meaburn et al. 1998; Meaburn & Boumis 2009). We also wished to draw attention to the fact that while the local velocity dispersion may exceed the globally averaged value, the latter is in turn an upper limit for the whole cloud.

#### 4.4 The mass-loss rate and lifetime

The time evolution of the core mass and various mass distributions have been previously discussed in Section 4.2.3. Here we note a more detailed examination of this mass-loss. In Fig. 18 the rate of mass-loss from the core is compared to the analytical formula for hydrodynamic ablation given by Hartquist et al. (1986). For this comparison we assume that the cloud is fully ionized with a radius  $r_c = 2$  pc, core density  $\rho_c = 4 \times 10^{-25}$  g cm $^{-3}$ , and temperature of 8000 K, and is in pressure equilibrium with the surrounding gas of density  $4 \times 10^{-28}$  g cm $^{-3}$  (i.e.  $\chi = 10^3$ ) and temperature  $8 \times 10^6$  K. Both the cloud and its surroundings are assumed to have solar abundances (average mass per particle,  $\mu = 0.61 m_H$ ). A shock of Mach number 1.5, 3, or 10, then travels through the ambient medium at a speed of 650, 1300, or 4300 km s $^{-1}$ , heating the medium to 12, 29, or 260 million K.

The analytical formula proposed by Hartquist et al. (1986) depends on the Mach number of the flow past the cloud. If this flow is supersonic (such as when the shock Mach number,  $M > 2.76$ ), then  $\dot{M}_{ab} \approx (M_c c_c)^{2/3} (\rho v)^{1/3}$ , while if the Mach number of the flow past the cloud,  $M_{ps}$ , is subsonic, then there is an additional  $M_{ps}^{4/3}$  dependence.  $M_c$  is the mass of the cloud,  $c_c$  is the sound speed within it, and  $\rho$  and  $v$  are respectively the density and velocity of the environment external to the cloud (the post-shock ambient/intercloud gas). With the above parameters,  $\dot{M}_{ab} \approx 1.1, 4.9, \text{ and } 8.2 \times 10^{-7}$  M $_{\odot}$  yr $^{-1}$  for interactions with Mach number 1.5, 3, and 10 shocks, and the cloud survives for approximately 1.8, 0.41, and 0.24 million yrs. In comparison the cloud crushing timescale,  $t_{cc} = 9.5, 4.8, \text{ and } 1.4 \times 10^4$  yrs, so that the cloud survives for about 18 cloud crushing timescales before being destroyed (clouds with a lower density contrast survive for a smaller multiple of  $t_{cc}$ ).

From Fig. 18 we see that the level of agreement between  $\dot{M}_{ab}$  and the numerically determined mass-loss rates from the simulations is reasonably good (gaps in the numerical curves indicate short periods when the cloud core accretes material). Furthermore, the rate of mass-loss from the core shows less extreme variations as the Mach number is reduced (i.e. the cloud is destroyed in a gentler fashion). However, the agreement shown in Fig. 18 is actually rather fortuitous, as we now demonstrate. The lifetime of the cloud,  $t_{life} = M_c / \dot{M}_{ab}$ , can be expressed in units of the cloud crushing timescale,  $t_{cc}$ , as

$$\begin{aligned} t_{life}/t_{cc} &= \left( \frac{M_c c_c}{\rho v} \right)^{1/3} \frac{M c_{amb}}{r_c c_c^{2/3} \chi^{1/2} [M_{ps}^{4/3}]} \\ &= 1.6 \left( \frac{\rho_c c_c}{\rho v} \right)^{1/3} \frac{M}{[M_{ps}^{4/3}]}, \end{aligned} \quad (13)$$

where the term in square brackets should only be used if the post-shock flow of density  $\rho$  and velocity  $v$  over the cloud is subsonic. As  $M \rightarrow \infty$ , because of the linear dependence of  $v$  on  $M$ , one finds that  $t_{life}/t_{cc} \propto M^{2/3}$ . For constant  $\rho_{amb}$  and  $c_{amb}$  (as in the simulations), Eq. 13 gives  $t_{life}/t_{cc} \propto (\rho_c c_c)^{1/3}$ , and, since  $\rho_c = \chi \rho_{amb}$  and  $c_c = \chi^{-1/2} c_{amb}$ , we find that  $t_{life}/t_{cc} \propto \chi^{1/6}$ .

The ratio of the core lifetime from the numerical models<sup>3</sup> to the lifetime assuming steady mass-loss at the rate

using the analytical formula of Hartquist et al. (1986) is shown in Fig. 19. The kink seen in the analytical curves at  $M = 2.76$  reflects the switch from Mach number dependent mass-loss when the postshock flow is subsonic ( $M < 2.76$  - i.e. the inclusion of the  $M_{ps}^{4/3}$  term in the above equations) to Mach number independent mass-loss when the postshock flow is supersonic. The displacement of the  $\chi = 10^2$  and  $\chi = 10^3$  curves reflects the  $\chi^{1/6}$  proportionality noted above.

The agreement for clouds with density contrasts  $\chi \sim 10^3$  hit by shocks with Mach numbers  $M \lesssim 10$  is again good, as was shown previously in Fig. 18. However, there is a significant and increasing divergence between the numerical and analytical cloud lifetimes as the shock Mach number increases past  $M = 15$ . For a Mach 40 shock, the numerical results indicate that the cloud is “destroyed” by  $t \approx 8 t_{cc}$ , whereas the analytical formula suggests a cloud lifetime of 20 – 40  $t_{cc}$  for  $\chi = 10 - 10^3$ , or up to 5 times longer. This is because of the  $M^{2/3}$  scaling of Eq. 13 at high Mach numbers. Note that the numerical results are consistent with Mach scaling (Section 3), whereas the analytical formula is not. Perhaps even more serious is the disagreement at moderate Mach numbers ( $M \lesssim 7$ ) and low density contrasts ( $\chi \sim 10$ ). In such cases the cloud survives appreciably longer than the analytical formula of Hartquist et al. (1986) suggests. For  $\chi = 10$  and  $M = 3$ , the analytical formula suggests that the cloud will survive until  $t = 4 t_{cc}$ , whereas the numerical calculation suggests the cloud actually survives until about  $t = 15 t_{cc}$  (i.e. its mass-loss rate is about 4 times lower than the equation in Hartquist et al. would suggest).

These differences have consequences for previous mass-loading calculations in which the analytical mass-loss rate prescription from Hartquist et al. (1986) was adopted (see, e.g., Dyson & Hartquist 1987; Arthur & Henney 1996; Strickland & Stevens 2000; Dyson, Arthur & Hartquist 2002). However, in practice, we believe that the results from such calculations will actually change very little, for a number of reasons. Firstly, mass-loading causes a flow’s Mach number to tend towards unity or thereabouts: supersonic flows are slowed as a result of momentum transfer and their temperature and sound speed increased through frictional heating, while subsonic flows are accelerated by mass-loading (see Eq. 5 in Hartquist et al. (1986), and the numerical calculations of Arthur, Dyson & Hartquist (1993)). This means that although use of the formula in Hartquist et al. (1986) for a cloud overrun by a high Mach number shock or immersed in a high Mach number flow results in the initial mass-loading being too slow, the rapid decrease in the Mach number of that flow in response to this mass-loading means that the analytically determined mass injection rate from clouds which are further downstream is closer to the correct (numerically determined) value. This behaviour is seen, for instance, in the mass-loading of the high Mach number pre-termination-shock stellar wind material in wind-blown-bubbles (Pittard, Hartquist & Dyson 2001a). It is also seen in the simulations of Arthur et al. (1993) and Arthur, Henney & Dyson (1996), where the position of the reverse shock of the wind-blown-bubble is fixed at the radius of the onset of mass-loading. Secondly, in

terial originally in the core has at least as much ambient material in each computational cell on the hydrodynamic grid.

<sup>3</sup> Defined as the time at which the core disappears - i.e. when ma-

most of these works values for the clouds (such as  $\chi$ ,  $r_c$ , etc.) were not explicitly specified. Instead, the authors simply adopt a constant rate of mass-injection into supersonic flow, modified by an  $M^{4/3}$  dependence for subsonic flow. Such simulations are therefore “exempt” from the large disparity between the analytical and numerical results for  $\chi \lesssim 10$  and  $M \lesssim 7$  which we have discovered in this work<sup>4</sup>.

Having established the existence of a large difference between the analytical and numerical lifetimes of clouds at high Mach numbers and at low-to-moderate Mach numbers for clouds with small density contrasts, we now wish to know the underlying cause of this discrepancy. For a flow streaming *supersonically* (i.e.  $M_{ps} > 1$ ) past a cloud, Hartquist et al. (1986) assumed that mass-loss occurs largely as a result of low pressure regions on the surface of the cloud. The mass-loss rate and lifetime of the cloud (in cgs units) is then found to be Mach number independent. However, this leads to a Mach number dependent lifetime for the cloud when expressed in units of  $t_{cc}$  (Eq. 13), since the dependence is introduced by  $t_{cc}$ . In contrast, the numerical simulations presented in this work (and earlier simulations in the literature) show that, for clouds with  $\chi \gtrsim 10^2$ , material is initially stripped from the sides of the cloud through the development of KH instabilities, while the core remains relatively intact. At later times, and at early times for clouds with  $\chi \lesssim 10$ , the instabilities break up the cloud into several large fragments. It seems reasonable to conclude, therefore, that the mass-loss process identified by Hartquist et al. (1986) is in fact not the dominant mode of mass-loss from deformable clouds subject to large velocity shear.

In contrast, Eq. 12 shows that the destruction time due to long wavelength KH instabilities has only a weak dependence on the shock Mach number. One finds that  $t_{KH} = 2.4 t_{cc}$  when  $M = 1.5$ , and  $t_{KH} = 1.33 t_{cc}$  when  $M = 40$ . These estimates are roughly 6 times shorter than the numerically determined lifetimes at high shock Mach number ( $M \gtrsim 7$ ). The scaling of the cloud lifetime (in units of  $t_{cc}$ ) with  $M$  is also weaker than is observed from the simulations (see Fig. 18). For instance, it predicts that the lifetime of a cloud hit by a Mach 1.5 shock is about 1.8 times longer than in a Mach 40 interaction. Nonetheless, the insensitivity of Eq. 12 to the cloud density contrast,  $\chi$ , is consistent with the numerical results, where only a weak (and non-monotonic) dependence is seen (Fig. 18). Given these observations, it seems reasonable to associate the mode of cloud destruction with KH instabilities, but it is clear that the lifetime of the cloud,  $t_{life} \sim 6 t_{KH}$ . This expression is within a factor of 2 or so of the numerically determined lifetime of clouds with  $10 < \chi < 10^3$  hit by shocks with

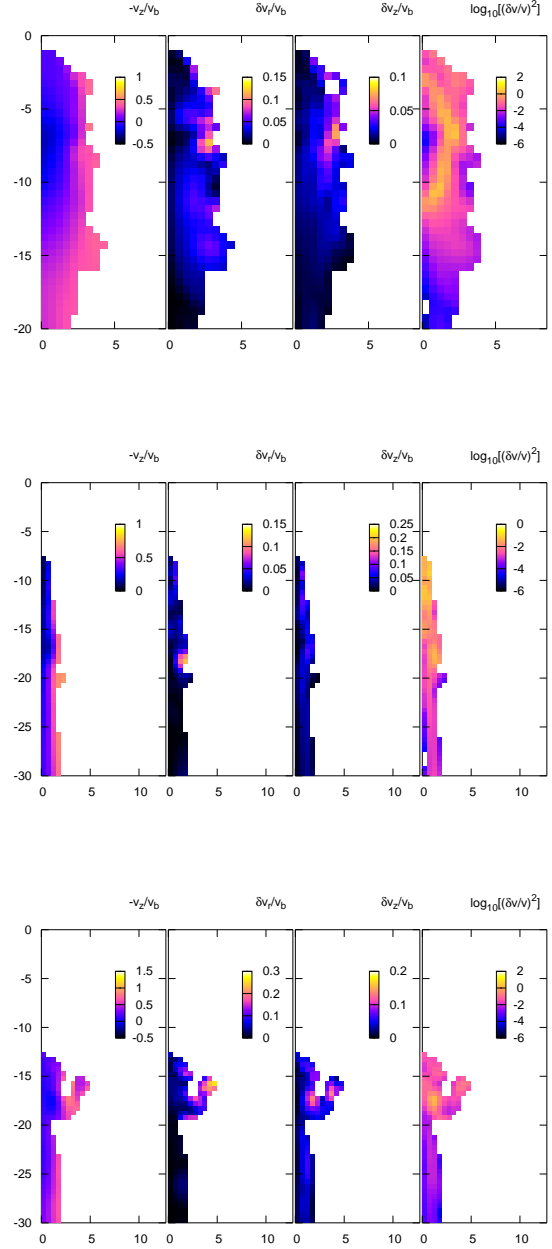


**Figure 17.** Snapshots of  $\langle v_z \rangle$ ,  $\delta v_r$ ,  $\delta v_z$ , and  $\log_{10}(\delta v/v)^2$ . In each pixel in these maps the mean axial velocity, the velocity dispersions, and the ratio of the energy in (resolved) turbulent motions to the kinetic energy of the mean flow are calculated from summing over many smaller hydrodynamic cells. The maps were constructed at  $t = 5.66 t_{cc}$  from simulations with  $\chi = 10^3$  and a)  $M = 1.5$  and b)  $M = 10$ . Panel c) shows the  $M = 10$  simulation at  $t = 7.10 t_{cc}$ , which is near the time of the peak value of the globally averaged  $\delta v_z$  (see Fig. 16f). The calculations were only performed in regions containing cloud material (i.e. where the colour in the above plots is other than white).

<sup>4</sup> Obviously other works examining different types of mass-loading in diffuse sources, for example through thermal conduction (e.g. McKee & Ostriker 1977; Chièze & Lazareff 1981; White & Long 1991; Pittard, Hartquist & Dyson 2001b; Pittard, Hartquist & Ashmore 2003a; Pittard et al. 2003b, 2004) or photoevaporation (e.g. García-Arredondo, Arthur & Henney 2002; Pittard et al. 2005), or where the mass-loading rate is unrelated to the properties of the local flow (e.g. Smith 1996; Dyson, Williams & Redman 1995; Williams, Hartquist & Dyson 1995; Williams, Dyson & Hartquist 1999), or is not from embedded clouds (e.g. Weaver et al. 1977; Toniazzo, Hartquist & Durisen 2001), remain unaffected.

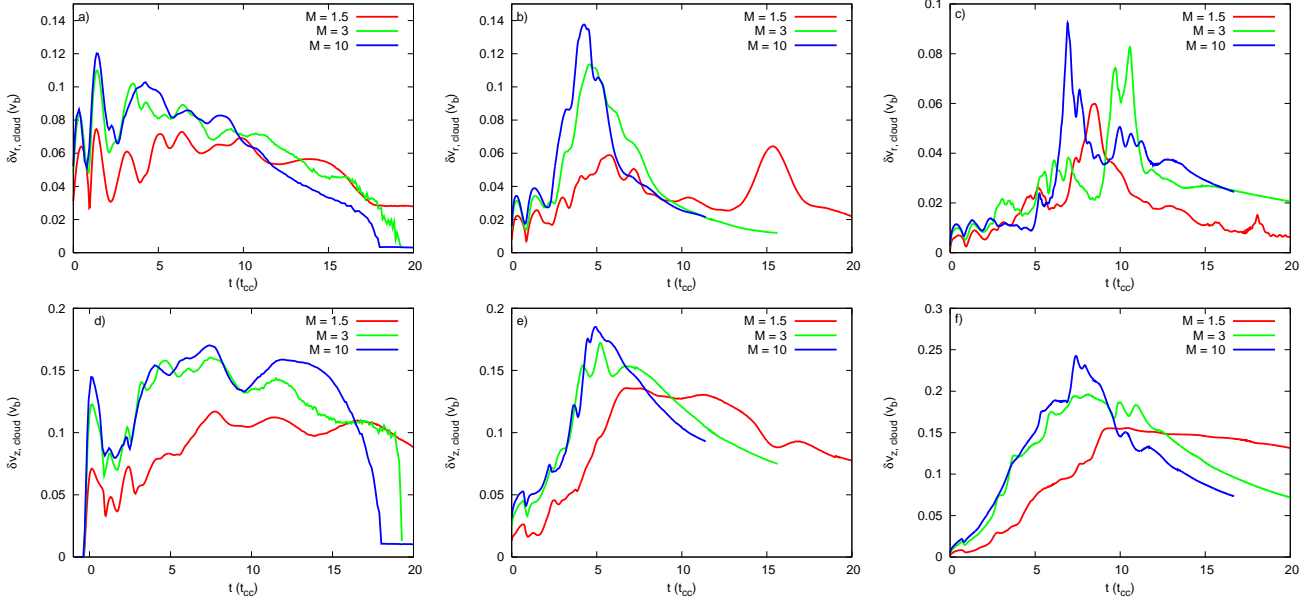


**Figure 16.** Top panels: Time evolution of the cloud velocity dispersion in the radial direction,  $\delta v_{r, \text{cloud}}$ , for various Mach numbers and density contrasts: (a)  $\chi = 10$ , (b)  $\chi = 10^2$ , (c)  $\chi = 10^3$ . Bottom panels: as the top panels, but for the velocity dispersion in the axial direction,  $\delta v_{z, \text{cloud}}$ .

**Table 4.** The parameters from least squares fits to  $t_{\text{drag}}/t_{cc}$  for the cloud (see Fig. 15a). The final column lists the sum of the residuals. In each case the fitted function has the form  $t_{\text{drag}}/t_{cc} = aM^b + c$ . Each fit has 4 degrees of freedom.

$\chi$	$a$	$b$	$c$	$\Sigma \text{ res}^2$
10	$5.11 \pm 0.35$	$-2.33 \pm 0.16$	$0.97 \pm 0.03$	0.0487
$10^2$	$7.94 \pm 0.84$	$-2.46 \pm 0.25$	$3.08 \pm 0.07$	0.043
$10^3$	$5.67 \pm 0.86$	$-0.66 \pm 0.34$	$4.84 \pm 1.04$	0.956

**Table 5.** The parameters from least squares fits to  $t_{\text{mix}}/t_{cc}$  for the cloud (see Fig. 15b). The final column lists the sum of the residuals. In each case the fitted function has the form  $t_{\text{mix}}/t_{cc} = aM^b + c$ . Each fit has 4 degrees of freedom.

$\chi$	$a$	$b$	$c$	$\Sigma \text{ res}^2$
10	$13.9 \pm 1.67$	$-2.90 \pm 0.28$	$6.00 \pm 0.09$	0.086
$10^2$	$6.93 \pm 0.69$	$-1.59 \pm 0.23$	$4.67 \pm 0.15$	0.135
$10^3$	$10.7 \pm 1.95$	$-1.10 \pm 0.43$	$6.11 \pm 0.96$	2.81

$M > 1.5$ , with the biggest discrepancy at low Mach numbers. The parameters of the fits to the numerical results are noted in Table 6.

## 5 SUMMARY AND CONCLUSIONS

This is the second of a series of papers investigating the turbulent destruction of clouds. In our first paper (Pittard et al. 2009) the focus was primarily on the much faster evolution and dispersal of a cloud over-run by a shock with a highly turbulent post-shock flow. Here we have performed a de-

**Table 6.** The parameters from least squares fits to  $t_{\text{life}}/t_{cc}$  for the cloud. The final column lists the sum of the residuals. In each case the fitted function has the form  $t_{\text{life}}/t_{cc} = aM^b + c$ . Each fit has 4 degrees of freedom.

$\chi$	$a$	$b$	$c$	$\Sigma \text{ res}^2$
10	$25.2 \pm 10.1$	$-1.89 \pm 1.06$	$10.1 \pm 2.00$	13.9
$10^2$	$20.3 \pm 4.94$	$-1.62 \pm 0.56$	$8.26 \pm 1.06$	6.52
$10^3$	$66.6 \pm 21.6$	$-2.82 \pm 0.76$	$10.2 \pm 1.20$	16.3

tailed examination of the Mach number dependence of the destruction of a cloud by an adiabatic shock. We have used a hydrodynamical code which incorporates a sub-grid compressible  $k-\epsilon$  turbulence model in an attempt to calculate the properties of the turbulence and the resulting increase in the transport coefficients.

We find that the most significant differences in the nature of the interaction occur between those where the ambient post-shock flow is subsonic with respect to the cloud, and those where it is supersonic (the latter requires that the shock Mach number  $M > 2.76$ ). For this reason, the interaction of a Mach 3 shock is more akin to a Mach 10 shock than a Mach 1.5 shock. At high Mach numbers the post-shock conditions are virtually independent of the Mach number and the so-called ‘‘Mach scaling’’ is obtained. Mach scaling appears to hold also when using the  $k-\epsilon$  turbulence model.

For weak shocks ( $M < 2.76$ ) the interaction is much milder and the following differences are observed: i) the postshock flow is subsonic with respect to the cloud, so a bowwave rather than a bowshock forms ahead of the cloud, ii) the compression of the cloud is more isotropic, iii) a weaker vortex ring is produced, iv) the smaller velocity difference at the slip surface around the cloud limits the KH

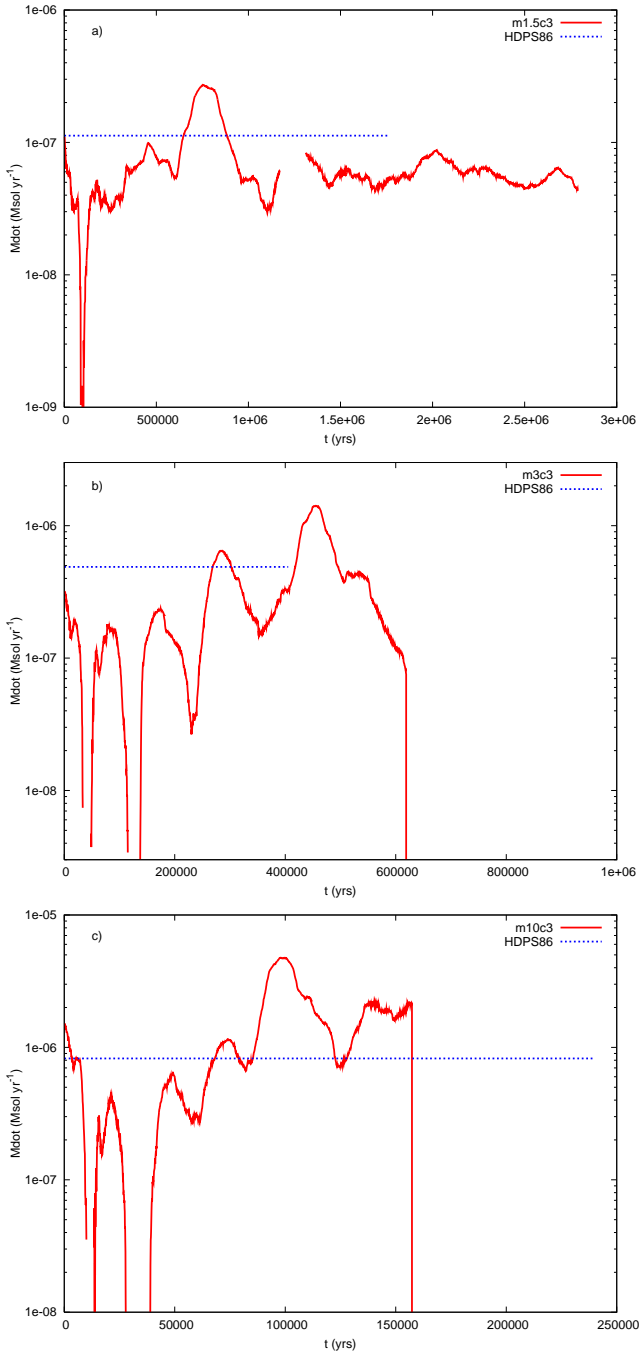


**Figure 18.** Mass loss rate for models with  $\chi = 10^3$  and a)  $M = 1.5$ , b)  $M = 3$ , and c)  $M = 10$ , compared to the mass-loss formula of Hartquist et al. (1986). Gaps in the curves indicate periods where the cloud core temporarily accretes material.

and RT instabilities and reduces the peak turbulent energy fraction of the flow, v) it takes much longer for the cloud to be mixed into the surrounding flow and for it to accelerate to the intercloud postshock speed, and vi) mass stripped from the cloud does not as readily form a long tail (the set-up time is longer). We further find that a prominent tail only forms if  $\chi \gtrsim 10^3$ .

Our most important finding is that the analytical prescription in Hartquist et al. (1986) for the ablative mass-loss

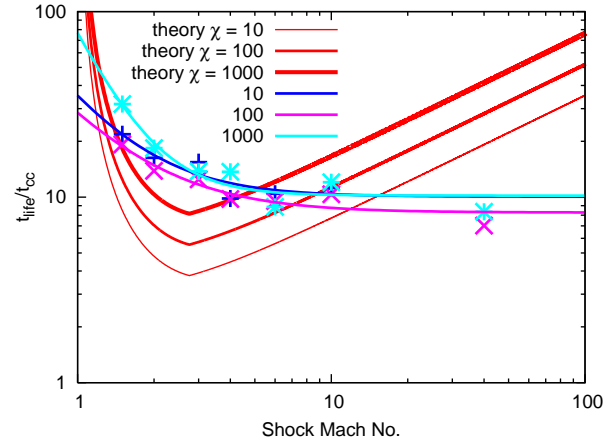


**Figure 19.** Comparison of the cloud lifetime from the numerical simulations (defined as the time when the “core” disappears) and the lifetime obtained from the analytical result of Hartquist et al. (1986), as a function of the shock Mach number,  $M$ , and the cloud density contrast,  $\chi$ .

rate of a cloud in an external flow predicts cloud lifetimes which are in disagreement with numerically determined values. For instance, the predicted lifetimes are a factor of 2–5 times too long for clouds with  $10 < \chi < 10^3$  hit by a Mach 40 shock, while they are about 4 times too short for clouds with  $\chi = 10$  hit by an  $M = 3$  shock. The reason for these discrepancies appears to be due to the assumption in Hartquist et al. (1986) that the mass-loss is mostly driven by pressure gradients around the cloud. Instead, we show that the cloud lifetime is more closely related to the timescale for large scale KH instabilities, though it is about 6 times longer than the latter. We argue, however, that the rapid reduction in the Mach number of hypersonic flows subject to mass-loading means that previous work in the literature is unlikely to greatly change if repeated using a more accurate mass-loss rate prescription.

In future work we will extend our investigation to three dimensions, examine the interaction of a dense shell with a cloud, and will compare synthetic signatures of the interaction to the types of diffuse sources mentioned in the introduction.

## ACKNOWLEDGEMENTS

We would like to thank the referee for a helpful report which improved this paper. JMP would also like to thank the Royal Society for funding a University Research Fellowship, and is grateful for useful discussions with John Dyson on some of this work.

## REFERENCES

- Arthur S. J., Henney W. J., 1996, *ApJ*, 457, 752
- Arthur S. J., Dyson J. E., Hartquist T. W., 1993, *MNRAS*, 261, 425
- Arthur S. J., Henney W. J., Dyson J. E., 1996, *A&A*, 313, 897



- Cecil G., Bland-Hawthorn J., Veilleux S., 2002, *ApJ*, 576, 745
- Chièze J. P., Lazareff B., 1981, *A&A*, 95, 194
- Conselice C. J., Gallagher J. S., Wyse R. F. G., 2001, *ApJ*, 122, 2281
- Cooper J. L., Bicknell G. V., Sutherland R. S., Bland-Hawthorn J., 2009, *ApJ*, 703, 330
- Danforth C. W., Blair W. P., Raymond J. C., 2001, *AJ*, 122, 938
- Dash S. M., Wolf D. E., 1983, AIAA paper 83-0704
- Dyson J. E., Hartquist T. W., 1987, *MNRAS*, 228, 453
- Dyson J. E., Arthur S. J., Hartquist T. W., 2002, *A&A*, 390, 1063
- Dyson J. E., Pittard J. M., Meaburn J., Falle S. A. E. G., 2006, *A&A*, 457, 561
- Dyson J. E., Williams R. J. R., Redman M. P., 1995, *MNRAS*, 237, 700
- Falle S. A. E. G., 1991, *MNRAS*, 250, 581
- Falle S. A. E. G., Coker R. F., Pittard J. M., Dyson J. E., Hartquist T. W., 2002, *MNRAS*, 329, 670
- Fragile P. C., Murray S. D., Anninos P., van Breugel W., 2004, *ApJ*, 604, 74
- García-Arredondo F., Arthur S. J., Henney W. J., 2002, *RMxAA*, 38, 51
- Gregori G., Miniati F., Ryu D., Jones T. W., 2000, *ApJ*, 543, 775
- Hartquist T. W., Dyson J. E., Pettini M., Smith L. J., *MNRAS*, 1986, 221, 715
- Klein R. I., McKee C. F., Colella P., 1994, *ApJ*, 420, 213
- Landau L. D., Lifshitz E. M., 1959, in “Fluid Mechanics” (Pergamon Press, Oxford)
- Levenson N. A., Graham J. R., Walters J. L., 2002, *ApJ*, 576, 798
- Mac Low M.-M., McKee C. F., Klein R. I., Stone J. M., Norman M. L., 1994, *ApJ*, 433, 757
- Marcolini A., Strickland D. K., D’Ercole A., Heckman T. M., Hoopes C. G., 2005, *MNRAS*, 362, 626
- Martin D. C., et al., 2007, *Nat*, 448, 780
- Matsuura M., et al., *ApJ*, 700, 1067
- McKee C. F., Ostriker J. P., 1977, *ApJ*, 218, 148
- Meaburn J., & Boumis P., 2009, *MNRAS*, in press
- Meaburn J., Clayton C. A., Bryce M., Walsh J. R., Holway A. J., Steffen W., 1998, *MNRAS*, 294, 201
- Melioli C., de Gouveia Dal Pino E. M., Raga A., 2005, *A&A*, 443, 495
- Mellema G., Kurk J. D., Röttgering H. J. A., 2002, *A&A*, 395, L13
- Miesch M. S., Zweibel E. G., 1994, *ApJ*, 432, 622
- Nakamura F., McKee C. F., Klein R. I., Fisher R. T., 2006, *ApJSS*, 164, 477
- Orlando S., Peres G., Reale F., Bocchino F., Rosner R., Plewa T., Siegel A., 2005, *A&A*, 444, 505
- Orlando S., Bocchino F., Reale F., Peres G., Pagano P., 2008, *ApJ*, accepted (arxiv:0801.1403)
- Patnaude D. J., Fesen R. A., 2005, *ApJ*, 633, 240
- Pittard J. M., 2007, in “Diffuse Matter From Star Forming Regions to Active Galaxies” (Springer-Verlag, Heidelberg)
- Pittard J. M., Arthur S. J., Dyson J. E., Falle S. A. E. G., Hartquist T. W., Knight M. I., Pexton M., 2003b, *A&A*, 401, 1027
- Pittard J. M., Dyson J. E., Falle S. A. E. G., Hartquist, 2005, *MNRAS*, 361, 1077
- Pittard J. M., Falle S. A. E. G., Hartquist T. W., Dyson J. E., 2009, *MNRAS*, 394, 1351
- Pittard J. M., Hartquist T. W., Ashmore I., 2003a, *A&A*, 408, 813
- Pittard J. M., Hartquist T. W., Dyson J. E., 2001a, *A&A*, 373, 1043
- Pittard J. M., Hartquist T. W., Ashmore I., Byfield A., Dyson J. E., Falle S. A. E. G., 2004, *A&A*, 414, 399
- Pittard J. M., Dyson J. E., Hartquist T. W., 2001b, *A&A*, 367, 1000
- Poludnenko A. Y., Frank A., Blackman E. G., 2002, *ApJ*, 576, 832
- Poludnenko A. Y., Frank A., Mitran S., 2004, *ApJ*, 613, 387
- Pope E. C. D., Pittard J. M., Hartquist T. W., Falle S. A. E. G., 2008, *MNRAS*, 385, 1779
- Raga A. C., Esquivel A., Riera A., Velázquez P. F., 2007, *ApJ*, 668, 310
- Shin M.-S., Stone J. M., Snyder G. F., 2008, *ApJ*, accepted (arXiv:0802.2708)
- Smith S. J., 1996, *ApJ*, 473, 773
- Stone J. M., Norman M. L., 1992, *ApJ*, 390, L17
- Strickland D. K., Stevens I. R., 2000, *MNRAS*, 314, 511
- Strickland D. K., Heckman T. M., Weaver K. A., Dahlem M., 2000, *AJ*, 120, 2965
- Toniazzi T., Hartquist T. W., Durisen R. H., 2001, *MNRAS*, 322, 149
- van Loo, S., Falle S. A. E. G., Hartquist T. W., Moore T. J. T., 2007, *A&A*, 471, 213
- Veilleux S., Cecil G., Bland-Hawthorn J., 2005, *ARA&A*, 43, 769
- Vieser W., Hensler G., 2007, *A&A*, 472, 141
- Weaver R., McCray R., Castor J., Shapiro P., Moore R., 1977, *ApJ*, 218, 377
- Westmoquette M. S., Gallagher J. S., Smith L. J., Tranco G., Bastian N., Konstantopoulos I. S., 2009, *ApJ*, accepted (arXiv:0907.3162)
- Westmoquette M. S., Smith L. J., Gallagher J. S. III, O’Connell R. W., Rosario D. J., De Grijs R., 2007, *ApJ*, 671, 358
- White R. L., Long K. S., 1991, *ApJ*, 373, 543
- Williams R. J. R., Dyson J. E., Hartquist T. W., 1999, *A&A*, 344, 675
- Williams R. J. R., Hartquist T. W., Dyson J. E., 1995, *ApJ*, 446, 759